Structure of the Entrainment Zone Capping the Convective Atmospheric Boundary Layer

PETER P. SULLIVAN, CHIN-HOH MOENG, BJORN STEVENS, DONALD H. LENSCHOW, AND SHANE D. MAYOR

National Center for Atmospheric Research, Boulder, Colorado*

(Manuscript received 22 August 1997, in final form 16 January 1998)

ABSTRACT

The authors use large-eddy simulation (LES) to investigate entrainment and structure of the inversion layer of a clear convectively driven planetary boundary layer (PBL) over a range of bulk Richardson numbers, Ri. The LES code uses a nested grid technique to achieve fine resolution in all three directions in the inversion layer.

Extensive flow visualization is used to examine the structure of the inversion layer and to illustrate the temporal and spatial interaction of a thermal plume and the overlying inversion. It is found that coherent structures in the convective PBL, that is, thermal plumes, are primary instigators of entrainment in the Ri range $13.6 \leq \mathrm{Ri} \leq 43.8$. At Ri = 13.6, strong horizontal and downward velocities are generated near the inversion layer because of the plume–interface interaction. This leads to folding of the interface and hence entrainment of warm inversion air at the plume's edge. At Ri = 34.5, the inversion's strong stability prevents folding of the interface but strong horizontal and downward motions near the plume's edge pull down pockets of warm air below the nominal inversion height. These pockets of warm air are then scoured off by turbulent motions and entrained into the PBL. The structure of the inversion interface from LES is in good visual agreement with lidar measurements in the PBL obtained during the Lidars in Flat Terrain field experiment.

A quadrant analysis of the buoyancy flux shows that net entrainment flux (or average minimum buoyancy flux $\overline{w\theta}_{\min}$) is identified with quadrant IV $\overline{w^-\theta^+} < 0$ motions, that is, warm air moving downward. Plumes generate both large negative quadrant II $\overline{w^+\theta^-} < 0$ and positive quadrant III $\overline{w^-\theta^-} > 0$ buoyancy fluxes that tend to cancel.

The maximum vertical gradient in potential temperature at every (x, y) grid point is used to define a local PBL height, $z_i(x, y)$. A statistical analysis of z_i shows that skewness of z_i depends on the inversion strength. Spectra of z_i exhibit a sensitivity to grid resolution. The normalized entrainment rate w_e/w_*, where w_e and w_* are entrainment and convective velocities, varies as $A\mathrm{Ri}^{-1}$ with $A \approx 0.2$ in the range $13.6 \leq \mathrm{Ri} \leq 43.8$ and is in good agreement with convection tank measurements. For a clear convective PBL, the authors found that the finite thickness of the inversion layer needs to be considered in an entrainment rate parameterization derived from a jump condition.

1. Introduction

Density interfaces are commonplace in geophysical flows and they often serve as boundaries between turbulent and nonturbulent fluid. For example, in the atmospheric planetary boundary layer (PBL) the daytime convectively unstable layer is generally capped by a nonturbulent stable layer. The growth of the convective layer is tied to the mixing process that occurs at the density interface (or inversion) between the well-mixed turbulent layer and the nonturbulent air in the capping stable layer. The process whereby stably stratified air from above is mixed into the developing convectively unstable PBL is entrainment. Although the entrainment process is common to nearly all turbulent flows, it is generally not well understood. From a practical perspective, the parameterization of entrainment is important but usually inadequate in most PBL models (e.g., Ayotte et al. 1996).

Despite the many studies focusing on entrainment, we do not yet have a clear picture of the physical mechanisms that determine the entrainment rate in the atmosphere. The entrainment rate, as defined here, is the time rate of change of the average PBL height in the absence of subsidence. Attempts to identify the basic building blocks of entrainment and hence entrainment rates through atmospheric observations are challenging; they are hindered by the variability of the atmosphere at larger scales, that is, mesoscale variations, and by the coupling between numerous physical processes, for example, cloud physics and large-scale gravity waves (Hauf and Clark 1989).

* NCAR is sponsored by the National Science Foundation.

Corresponding author address: Dr. Peter P. Sullivan, MMM Division, NCAR, P.O. Box 3000, Boulder, CO 80307-3000.
E-mail: pps@ncar.ucar.edu

In order to gain insight into entrainment mechanics, numerous laboratory studies have attempted to model an idealized entrainment process via small-scale ''mixing-box'' and convection tank experiments. In the mixing-box experiments entrainment occurs at an imposed density interface due to turbulence generated by an oscillating grid. Some recent relevant studies are Hannoun and List (1988), Perera et al. (1994), and Kit et al. (1997); Fernando (1991) provides a current review. Perera et al. (1994) found that the theoretical model of Carruthers and Hunt (1986) partially explained some of their experimental results. One of the conclusions from this body of literature is that the entrainment mechanism depends on the local Richardson number $\mathrm{Ri}_l = N_i^2 L_H^2/u_H^2$, where N_i is the buoyancy frequency of the inversion, and L_H and u_H^2 are the integral length scale and variance of the turbulence in the absence of the density interface. They found that the main entrainment mechanism at low Ri_l, say $\mathrm{Ri}_l \leq 15$, is large-scale engulfment by turbulent eddies; this gives way to intermittent wave breaking at $\mathrm{Ri}_l \geq 20$ and finally to molecular diffusion at very large Ri_l, $\mathrm{Ri}_l > 60$. However, it is difficult to extrapolate these results to the atmosphere because of the great disparity in Reynolds number. Perhaps an even more important difference between these mixing-box experiments and the PBL is the assumed analogy between grid-generated and convective PBL turbulence. This assumption is questionable since the atmosphere is known to contain large-scale coherent structures, that is, thermal plumes, that control the PBL dynamics. These structures are absent in mixing-box experiments.

The thermally driven convection tank simulations of Deardorff et al. (1980), obtained at larger Reynolds number, are a closer analog to PBL turbulence. They correlated the entrainment rate to a bulk Richardson number,

$$\mathrm{Ri} = g\beta\Delta\theta\,\overline{z_i}/w_*^2, \tag{1}$$

based on the temperature jump $\Delta\theta$, the average PBL height $\overline{z_i}$, the convective velocity scale w_*, gravity g, and coefficient of thermal expansion β. Equation (1) can also be written as

$$\mathrm{Ri} = \Delta\theta/\theta_*, \tag{2}$$

where the convective velocity scale $w_* = (g\beta Q_o\overline{z_i})^{1/3}$, the temperature scale $\theta_* = Q_o/w_*$, and Q_o is the surface heat flux. For Ri values typical of the atmosphere Deardorff et al. (1980) found the dimensionless entrainment rate to vary as

$$\frac{w_e}{w_*} = \frac{A}{\mathrm{Ri}}, \tag{3}$$

where w_e is the entrainment velocity and A is a parameter in the range $0.1 < A < 0.2$. The data spread does not permit choosing between different Ri power laws and other studies have shown that the parameter A varies with shear (Moeng and Sullivan 1994). For radiatively driven PBLs the validity of Eq. (3) is currently being debated. Moeng et al. (1998, manuscript submitted to *J. Atmos. Sci.*) suggest that Eq. (3) needs to be corrected for radiation, while the laboratory experiments of Sayler and Breidenthal (1998) and the large-eddy simulation of Stevens and Bretherton (1998) find that Eq. (3) is valid over a wide range of Ri.

In this investigation, we use large-eddy simulation (LES) to study entrainment mechanics in an atmospheric PBL. LES has been successfully used in the past to study numerous aspects of PBL turbulence (e.g., Wyngaard 1984) and, to a much lesser degree, entrainment (e.g., Sorbjan 1996). The recent work of Bretherton et al. (1998) provides some justification for our use of LES. They showed that different LES models predicted similar entrainment rates for radiatively driven PBLs independent of the subgrid-scale (SGS) model and numerics provided that the vertical grid size was fine enough to resolve the horizontal variability of the local inversion height. In the current investigation, fine meshes are used in all directions in the entrainment zone and the Richardson numbers considered are small compared to the radiatively driven PBL studied by Bretherton et al. (1998). This gives us confidence in the application of LES for the study of PBL entrainment. The objectives of the present work are to elucidate the structure of the inversion interface, identify possible entrainment mechanisms, and compare the inversion layer structure across a range of Richardson numbers for a series of clear convectively driven PBLs.

2. The LES code

The LES code used here was originally developed by Moeng (1984) and has since undergone continuous development. Recently, Sullivan et al. (1996) added a grid-nesting capability that allows grid refinement in a selected region of the computational domain. Two-way interaction between the outer (coarse) and nested (fine) meshes is accounted for and the same numerical methods are used on each mesh. The nested mesh covers the same horizontal dimensions as the outer grid, but its vertical extent is variable. In the present study, the grid refinement is placed in the entrainment zone as described in section 3. Periodic boundary conditions are used in the horizontal directions, Monin–Obukhov similarity theory is used to construct the lower boundary conditions (Moeng 1984), and radiation boundary conditions (Klemp and Durran 1983) are used at the top of the domain to allow gravity waves to escape.

In order to further test the computed solution's sensitivity to the numerical method, an option to use a second-order upwind scheme for vertical scalar advection operators has also been added to the code. This flux-corrected upwind scheme (Beets and Koren 1996; Koren 1993), which is monotone, prevents unrealizable oscillations that are present with second-order centered schemes in regions of large vertical scalar gradients. We

TABLE 1. Simulations and grid resolutions.

Case	Coarse-mesh grid points	Coarse-mesh spacing (Δx, Δy, Δz)m	Fine-mesh grid points	Fine-mesh spacing (Δx, Δy, Δz)m
W06	$50^2 \times 100$	100, 100, 20	$150^2 \times 40$	33.3, 33.3, 10.0
W05	$50^2 \times 100$	100, 100, 20	$150^2 \times 40$	33.3, 33.3, 10.0
W04	$50^2 \times 100$	100, 100, 20	$150^2 \times 40$	33.3, 33.3, 10.0
W02	$50^2 \times 100$	100, 100, 20	$150^2 \times 40$	33.3, 33.3, 10.0
S45	$50^2 \times 100$	100, 100, 20	$150^2 \times 36$	33.3, 33.3, 10.0
S40	$50^2 \times 100$	100, 100, 20	$150^2 \times 36$	33.3, 33.3, 10.0
S35	$50^2 \times 100$	100, 100, 20	$150^2 \times 36$	33.3, 33.3, 10.0
S30	$50^2 \times 100$	100, 100, 20	$150^2 \times 36$	33.3, 33.3, 10.0
S24	$50^2 \times 100$	100, 100, 20	$150^2 \times 36$	33.3, 33.3, 10.0
W06/c	$50^2 \times 100$	100, 100, 20	none	none
S24/c	$50^2 \times 100$	100, 100, 20	none	none
S24/m	$50^2 \times 100$	100, 100, 20	none	none
S24/sd	$50^2 \times 100$	60, 60, 20	$200^2 \times 54$	15, 15, 6.67

TABLE 2. Properties of simulations.

Case	Q_o K m s^{-1}	w^* m s^{-1}	$\overline{z_i}$ m	τ s	Ri	w_e cm s^{-1}	$\Delta\theta$ K
W06	0.060	1.34	1230	918	13.6	2.73	0.607
W05	0.050	1.25	1203	962	14.5	2.18	0.578
W04	0.041	1.17	1170	1000	15.2	1.57	0.543
W02	0.020	0.89	1086	1217	19.4	0.64	0.436
S45	0.450	2.56	1145	447	19.2	2.61	3.37
S40	0.400	2.46	1133	460	24.7	2.18	4.03
S35	0.350	2.34	1121	479	22.7	1.86	3.40
S30	0.300	2.21	1100	498	25.7	1.57	3.49
S24	0.240	2.04	1084	531	34.5	1.27	4.06
W06/c	0.060	1.36	1286	946	13.3	3.09	0.586
S24/c	0.240	2.05	1096	535	34.1	1.27	4.00
S24/m	0.240	2.05	1094	534	31.6	1.34	3.70
S24/sd	0.240	2.03	1071	528	43.8	1.26	5.17

adopted the SGS model proposed by Deardorff (1980), implemented by Moeng (1984), and modified by Sullivan et al. (1994). This grid-nesting code has been used to study surface-layer processes in both the atmosphere (Sullivan et al. 1996) and ocean (McWilliams et al. 1997), and to study radiatively driven PBLs (Moeng et al. 1998, manuscript submitted to *J. Atmos. Sci.*).

3. The LES experiments

In this study, only free convective flows are considered; that is, the PBL is driven solely by a surface heat flux. A series of LESs with varying PBL inversion strengths and surface heat flux forcing were carried out with fine grid resolution in the entrainment zone. In addition, a limited number of grid resolution experiments along with a monotone advection scheme were used to test the solution's sensitivity to the numerical procedure.

For any particular simulation, the initial potential temperature soundings, that is, $\theta(z)$, were constructed from a three-layer structure: a constant potential temperature in the mixed layer, a finite θ jump across the inversion, and a uniform lapse rate above the inversion. In order to achieve a range of Ri (note Ri $= \Delta\theta/\theta_*$), two initial θ jumps were considered: a weak jump of less than 1 K, which is typical of a midmorning PBL during a rapid growth phase, and a strong jump of more than 6 K that corresponds to a PBL with warm air advection aloft or strong subsidence. The shape of the temperature profile in our simulations, after the initialization, is a slowly varying function of time due to surface heating.

The LES computational domain was covered by a modest resolution mesh over the bulk of the PBL with a much finer-resolution mesh near the capping inversion. The vertical location of the nested mesh was chosen so that the PBL top was positioned near the vertical center of the nested mesh. Since the grid-nesting scheme is not adaptive, the upper and lower boundaries of the nested mesh were chosen prior to run time based on the expected growth of the PBL. For efficient computer usage, the general strategy was to start each run from the same random initial conditions and run for more than 10 large-eddy turnover times on the coarse mesh to establish a statistically steady turbulent flow. At that point, the nested fine mesh calculations were turned on and the run was continued for an additional four turnover times.

Three-dimensional data volumes were archived from the later stages of the simulations to gather statistics and carry out flow visualization. The ensemble mean and turbulence statistics shown here are the result of either spatial, that is, at a fixed z location averaging over an x–y plane (indicated by $\langle\ \rangle$), or spatial and temporal averaging (indicated by $\overline{(\ )}$). Typically, 20 data volumes were used to compute the temporal averages.

The mesh resolution and bulk properties of the various simulations are listed in Tables 1 and 2. Here, the name of a particular simulation (or case) is taken from the strength of the inversion jump—either weak (W) or strong (S)—and the numerical value of the surface heat flux; for example, S24 is a simulation with a strong overlying inversion and surface heat flux of 0.24 K m s^{-1}.

In these tables, (Δx, Δy, Δz) are the coarse and fine mesh spacings in the (x, y, z) coordinate directions, Q_o is the surface heat flux used to drive the PBL, $w_* = (gQ_o\overline{z_i}\beta)^{1/3}$ is the convective velocity scale, $\overline{z_i}$ is the temporally and spatially averaged PBL depth based on the maximum vertical θ gradient (see section 4), $\tau = \overline{z_i}/w_*$ is the large-eddy turnover time, Ri is a bulk Richardson number defined by Eq. (1), w_e is the entrainment velocity (see section 7b for details of its computation), and $\Delta\theta$ is the average jump across the inversion defined as the θ jump between the position of the minimum buoyancy flux and the height where the heat flux vanishes.

For all simulations, the outer computational domain was 5 km $\times$ 5 km $\times$ 2 km except for case S24/sd, which had a smaller horizontal domain of 3 km $\times$ 3 km $\times$ 2 km. The vertical extent of the nested mesh varied from

360 to 400 m depending on the inversion strength (cases with weaker inversions had the larger vertical extent).

Some exploration was done to test the solutions' sensitivity to grid resolution, domain size, and numerical scalar advection operator. These numerical experiments are indicated by an additional suffix, ''/c'' for coarse grid only, ''/m'' for monotone advection scheme on a coarse grid, and ''/sd'' for a smaller domain. These exploratory runs are in no way exhaustive but were performed to show that the baseline solutions were not unduly sensitive to numerical parameters.

4. Definition of PBL height

The height of the boundary between the PBL mixed layer and the stably stratified layer, referred to as z_i, is one of the defining characteristics of the PBL and in particular the entrainment zone. Here z_i is used as a length scale to compare different PBLs and its statistical properties are also used to quantify the inversion characteristics. In the present study, we compare four different definitions for the PBL height.

a. Flux methods

In the standard flux method, the PBL height z_{i1} is defined as the vertical location of the average minimum heat flux

$$z_{i1} = z, \quad \text{where} \quad \langle w\theta(z)\rangle \text{ is minimum.} \tag{4}$$

In order to compute z_{i1}, we first form the 3D flux array $w\theta(x, y, z)$, then apply the horizontal averaging operator to produce $\langle w\theta(z)\rangle$, and finally search through this array to locate the minimum flux $\langle w\theta(z)\rangle_{\min}$. The vertical location of $\langle w\theta(z)\rangle_{\min}$ is defined as the PBL height z_{i1}. This definition of the PBL height was introduced by Deardorff et al. (1980) and is often used in LES. One of its virtues is that z_{i1} can be easily and unambiguously computed in an LES. However, drawbacks of this method are that at any given time spatial variations in the PBL height are ignored since the layer-averaged heat flux is used and $\langle w\theta\rangle_{\min}$ is difficult to measure in the field. As we will show later (see section 6) the PBL height has large spatial variability.

In order to improve on the standard flux method a slight variant was considered that takes into account some of the spatial variability of the PBL height. In the modified flux method, the PBL height z_{i2} is defined as in Eq. (4) but from a x-averaged heat flux profile $[w\theta(y, z)]$, where the operator [ ] denotes x averaging. Only a single x–z plane of data at a fixed y is used to form $[w\theta(y, z)]$. Hence we can obtain multiple estimates of the PBL height at all y locations according to the rule

$$z_{i2}(y) = z, \quad \text{where} \quad [w\theta(y, z)] \text{ is minimum.} \tag{5}$$

Since N_y slices of data are available, N_y estimates of z_{i2} can be computed at any particular time.

b. Contour method

The contour method is commonly used in mixing-box experiments to define entrainment rates (e.g., Hannoun and List 1988). In these experiments, the entrainment interface is defined by tracking the vertical location of a scalar contour in the entrainment zone on a point-by-point basis. For our purposes, we track the vertical location of a constant virtual potential temperature contour θ_{con} in the PBL. The PBL height $z_{i\theta}$ is then the solution of

$$z_{i\theta}(x, y) = z, \quad \text{where} \quad \theta(x, y, z) = \theta_{\text{con}}. \tag{6}$$

In our implementation, the searching algorithm begins at the top of the domain and locates the first occurrence of the selected contour.

The contour method provides more information about the entrainment interface since it accounts for pointwise horizontal variations. However, knowledge of which specific contour θ_{con} to track needs to be known a priori. The choice of θ_{con} is problem dependent, varying with the strength of the capping inversion. Another disadvantage is that the entrainment interface is not characterized by a single contour and the temperature contours, which as a group form the entrainment zone, evolve as time progresses. In other words, for a given contour that lies in the entrainment zone at time $t = t_1$ this same contour may no longer be representative of the entrainment dynamics at some later time $t = t_2$ since the PBL will have grown because of surface heating. As a consequence, entrainment rates based on tracking a specific contour are lower than those that actually follow the entrainment interface.

c. Gradient method

In the gradient method, the PBL height z_{ig} is defined as the vertical location of the largest increase in potential temperature, that is, the vertical position of the maximum θ gradient. For any particular position (x, y) the PBL height is the location where

$$z_{ig}(x, y) = z, \quad \text{where} \ \frac{\partial\theta(x, y, z)}{\partial z} \text{ is maximum.} \tag{7}$$

In our implementation of Eq. (7), we compute vertical θ gradients using a centered difference at each horizontal grid point and search vertically [at constant (x, y)] to find the maximum. The vertical location of the maximum gradient is then defined as z_{ig}. The gradient method has advantages compared to the previous methods: the local spatial variation of the PBL height is preserved, the method can be applied without prior knowledge of a specific θ contour to track, and the method follows the interface as it evolves in time. Our gradient method is closely related to the wavelet technique used by Mann et al. (1995) to identify the PBL inversion height in field experiments.

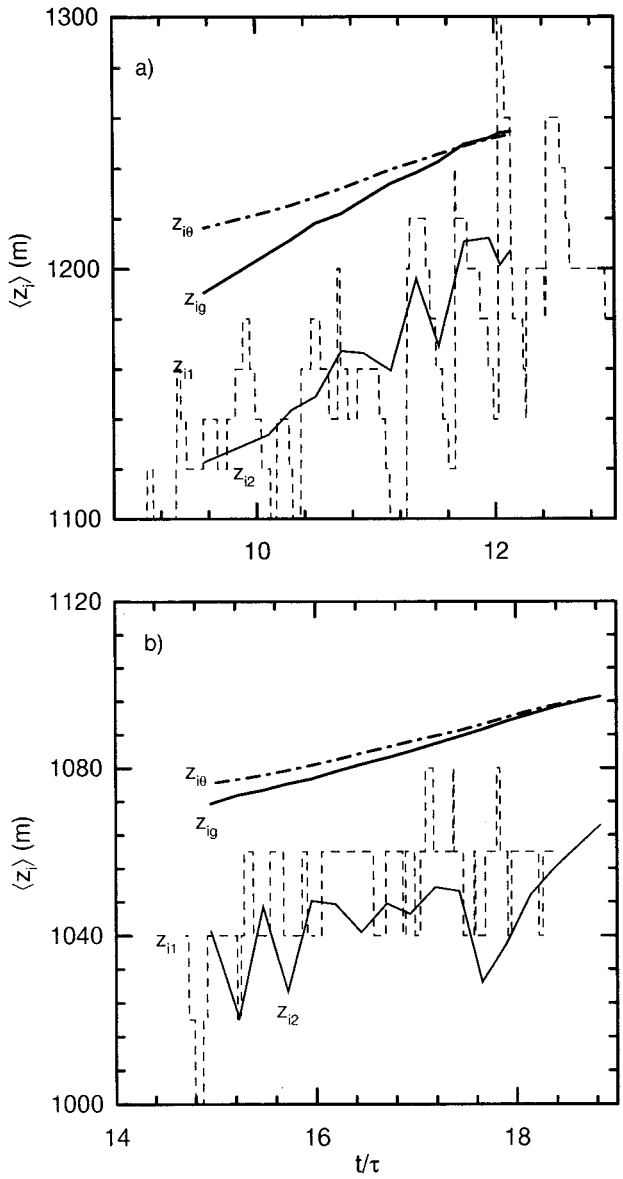

FIG. 1. Comparison of PBL height $\langle z_i \rangle$ vs dimensionless time t/τ estimated with different methods for cases (a) W06 and (b) S24. Here, z_{i1} is average flux method, z_{i2} is modified flux method, $z_{i\theta}$ is contour method, and z_{ig} is gradient method.

d. Comparison of z_i methods

A comparison of all four z_i methods is shown in Fig. 1 for simulations W06 and S24; note that layer-averaged values of z_i are plotted for modified flux, contour, and gradient methods. Inspection of these figures shows that the standard flux method has large temporal fluctuations and generally predicts a value of $\langle z_i \rangle$ smaller than either the contour or gradient methods. In the standard flux method, $\langle z_i \rangle$ is determined from a single spatial estimate and hence displays a large temporal variability. We should note that for PBLs with stronger inversions it is difficult to discern the temporal trend of $\langle z_i \rangle$ from the flux method, as shown in Fig. 1b. The modified flux method yields a noticeably smoother variation of $\langle z_i \rangle$ and, as expected, generally tracks a ''best fit'' to the $\langle z_i \rangle$ data obtained from the standard flux method. Smooth estimates for $\langle z_i \rangle$ are obtained from the contour and gradient methods because they are local methods and thus use a larger statistical sample to estimate $\langle z_i \rangle$. The specific contour used in the contour method was selected after the data had initially been reduced and was chosen to follow the entrainment zone at a late time in the simulation. Notice that, in Fig. 1a, the slope of the $\langle z_i \rangle$ versus t curve for the gradient method is steeper by more than 60% compared to the contour method (hence the entrainment rate estimated from the gradient method is likewise greater). The steeper slope from the gradient method is due to the continual advancement of the entrainment interface through the temperature field with time. The difference in $\langle z_i \rangle$ versus t slopes predicted by the gradient and contour methods is greatest for PBLs with relatively weak inversions where the interface location grows substantially with time. Note that the slope of the curve obtained from the modified flux method is comparable to that of the gradient method. This is consistent with the laboratory investigation of Deardorff et al. (1980), who found that the height of the minimum average heat flux was always below the uppermost height reached by the most vigorous thermals, but the lines tracking the minimum average heat flux and the height of the maximum thermal penetration were, however, generally parallel. Our definition of z_i based on the maximum vertical gradient in θ is slightly below the height reached by the strongest thermals but above the height of the minimum average heat flux. We have adopted the gradient method as our definition of the PBL height since it is consistent with the flow visualization shown later in section 6a and because we feel z_{ig} is representative of the entrainment interface dynamics. Hereafter, when we refer to z_i we are using the gradient method and $z_i(x, y) = z_{ig}(x, y)$. Also, $\langle z_i \rangle$ is the spatial horizontal average at a particular time and $\overline{z_i}$ denotes both a spatial and temporal average.

5. Low-order flow statistics

Typical vertical profiles of the average virtual potential temperature, that is, $\overline{\theta}$ versus $z/\overline{z_i}$, are shown in Fig. 2 for simulations W06 and S24, which are characterized by different overlying stratifications. These statistics are obtained by spatial and temporal averaging as mentioned in section 3. In Fig. 2a, the initial temperature sounding (indicated by the thin line) is also shown. Figure 2 shows that as time progresses a third layer develops in the inversion region with a maximum gradient, $\partial\overline{\theta}/\partial z$, larger than the initial sounding. This sharpening of the inversion strength, which results from entrainment, is also reported by Schmidt and Schumann (1989) and in mixing-box experiments (e.g., Perera et al. 1994). Also shown in Fig. 2 are the upper and lower boundaries

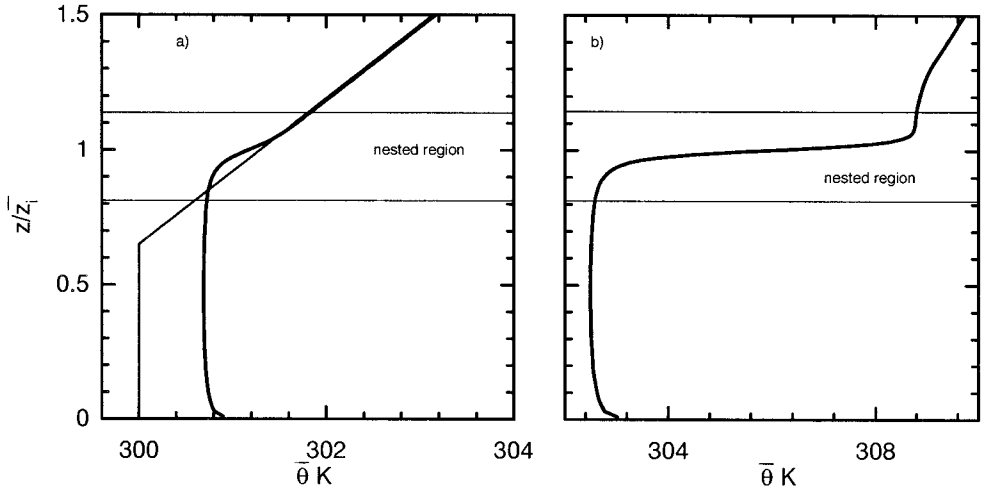

FIG. 2. Vertical profiles of average potential temperature $\overline{\theta}$ for cases (a) W06 and (b) S24. The upper and lower z boundaries of the nested grid are indicated by horizontal lines. In (a) the initial temperature sounding for the LES is shown by the thin lines.

of the nested grid. A smooth transition of the flow field and its statistics between the coarse and nested meshes was obtained in all cases.

In Fig. 3, normalized average heat flux profiles $\overline{w\theta}/Q_o$ are displayed. The total flux decreases linearly with height from the ground to the point where $\overline{w\theta}$ is a minimum. This linear behavior indicates that the flow has reached a quasi-steady state. Notice also that in the entrainment zone the SGS heat flux is small compared to the resolved heat flux, suggesting that the SGS effects are negligible except very close to the surface.

Vertical profiles of the normalized resolved velocity variances $(\overline{u'^2}, \overline{v'^2}, \overline{w'^2})/w_*^2$ and the SGS energy $2\overline{e}/3w_*^2$ depicted in Fig. 4 provide a sense of the overall turbulence properties in these simulations. For cases W06 and S24, the velocity variance profiles normalized by w_*^2 are similar in shape and magnitude for $z/\overline{z_i} < 0.7$. For $z/\overline{z_i} > 0.7$, the normalized horizontal velocity variances from these simulations are different, varying with the strength of the inversion. PBLs topped by stronger inversions produce larger horizontal velocity variances because a greater percentage of the upward motion in the thermals is transferred to the horizontal velocity components. The SGS energy is a small fraction of the resolved velocity variances. Vertical profiles of the normalized resolved potential temperature variance $\overline{\theta'^2}/\theta_*^2$, where $\theta_* = Q_o/w_*$, are displayed in Fig. 5. The potential temperature variance reaches a sharp maximum in the entrainment zone because of the mean gradient in potential temperature. The magnitude of this peak increases with increasing stratification. Notice that the height where the maximum occurs is located at $z =$

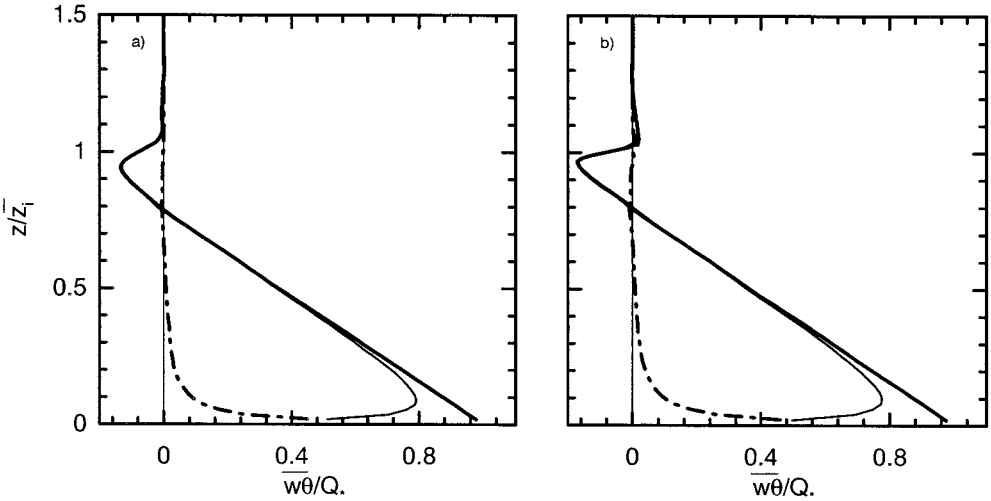

FIG. 3. Vertical profiles of average normalized heat flux $\overline{w\theta}/Q_o$ for cases (a) W06 and (b) S24. Solid line total heat flux, thin line resolved heat flux, and dash-dotted line SGS heat flux.

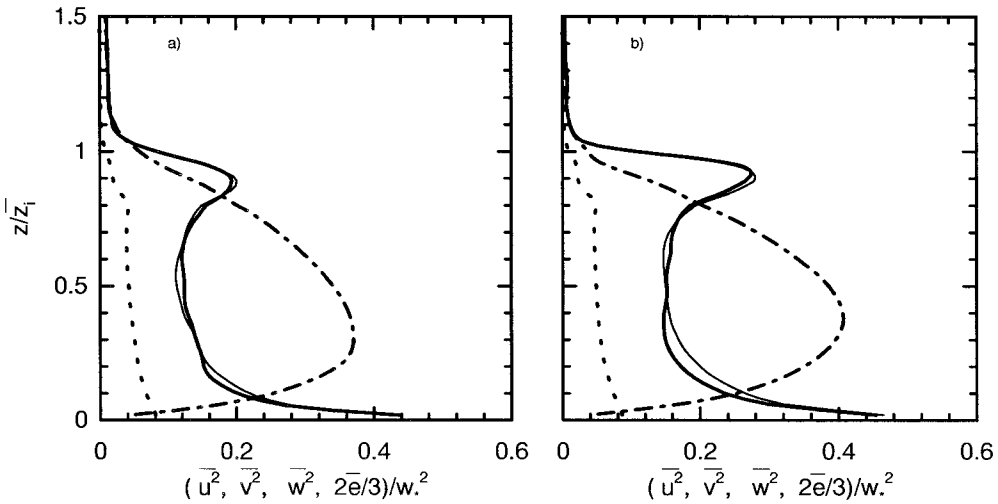

FIG. 4. Profiles of average normalized velocity variances and SGS energy for cases (a) W06 and (b) S24. Thick line u^2, thin line v^2, dash-dotted line w^2, and dotted line SGS e.

$\overline{z_i}$, where $\overline{z_i}$ is computed using the gradient method, and above the position of average minimum heat flux $\overline{w\theta}_{\min}$. Thus, from the perspective of potential temperature $z = \overline{z_i}$ is the location of the most intense temperature fluctuations in the entrainment zone. Overall, the present results agree quite well with prior computations (Moeng and Wyngaard 1989) and convection tank measurements (Deardorff and Willis 1985).

6. Description of entrainment events

The main objectives of the current study are to examine the structure of the inversion layer, identify possible entrainment mechanisms, and compare the inversion-layer structure across a range of Richardson numbers. Extensive visualization of the LES flow fields was carried out with these objectives in mind.

a. Visualization of low Richardson number flow, Ri = 13.5

The dominant coherent structures in a convectively driven PBL are large-scale thermal plumes as shown by many LESs (e.g., Schmidt and Schumann 1989) and observations (Lenschow 1970). These coherent structures are responsible for most of the turbulent transport and control the dynamics of the PBL. In view of the importance of plumes, it is natural to examine their role in the entrainment process.

A snapshot of the instantaneous vertical velocity field w and fluctuating potential temperature $\theta' = \theta - \langle\theta\rangle$ in an x–y plane at $z/\overline{z_i} = (1.05, 0.98, 0.89)$ is shown in Fig. 6 for case W06 (note only results from the nested region are shown). The dark (light) shading in this picture highlights regions of large positive (negative) fluc-

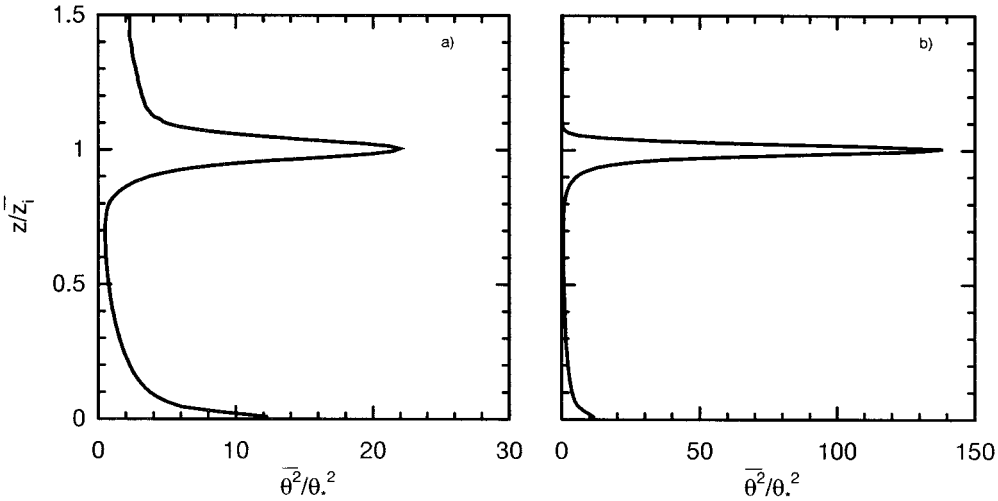

FIG. 5. Profiles of average normalized potential temperature variance for cases (a) W06 and (b) S24.

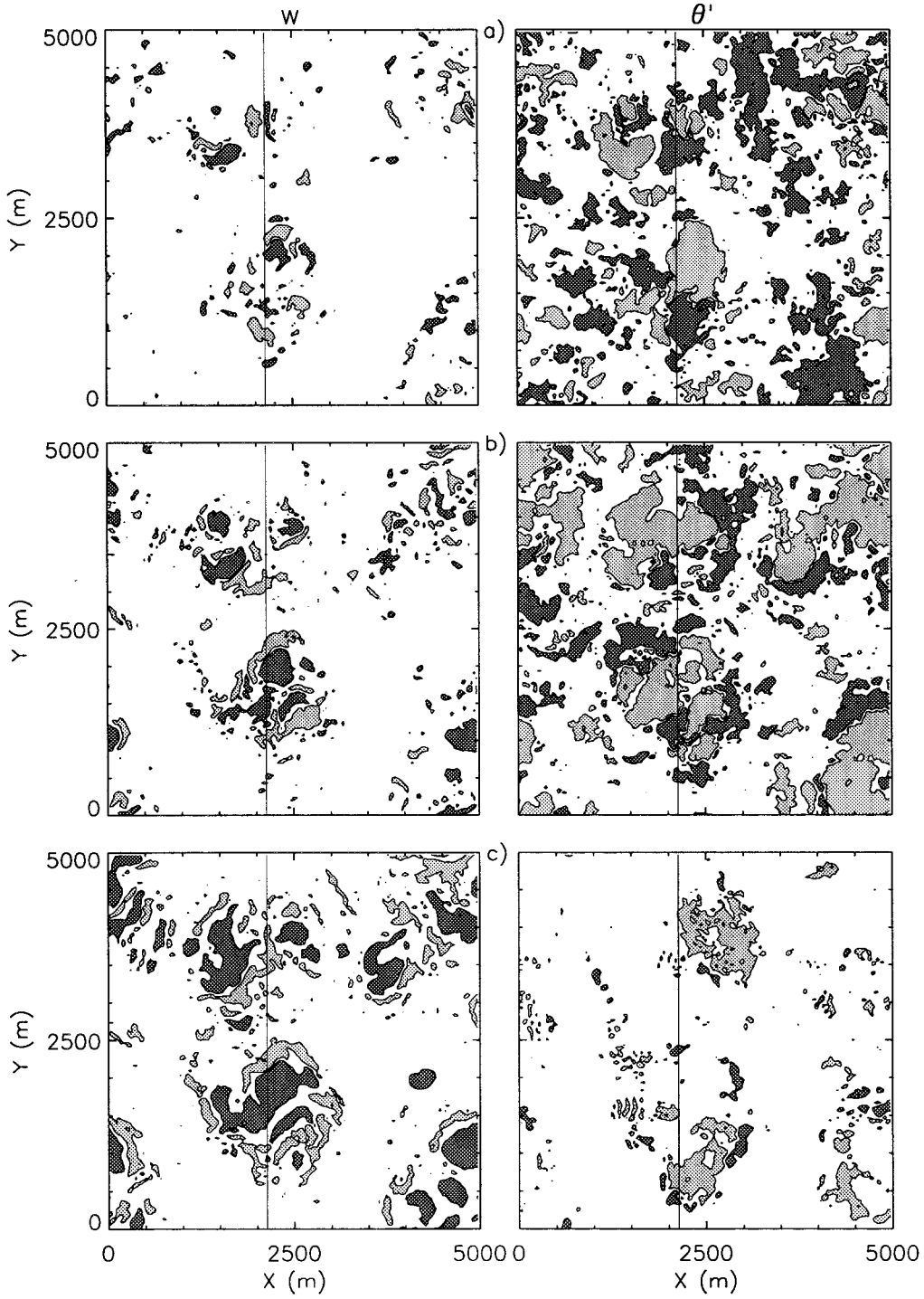

FIG. 6. Snapshot of vertical velocity w and potential temperature fluctuations θ' in an x–y plane for case W06 at vertical locations $z/\overline{z_i}$ = (a) 1.06, (b) 0.98, and (c) 0.89. Dark (light) shading indicates $w > 0.5$ m s^{-1} ($w < -0.5$ m s^{-1}), and $\theta' > 0.12$ K ($\theta' < -0.12$ K). Thin vertical line at $x = 2167$ m is the vertical cross section shown in Fig. 7.

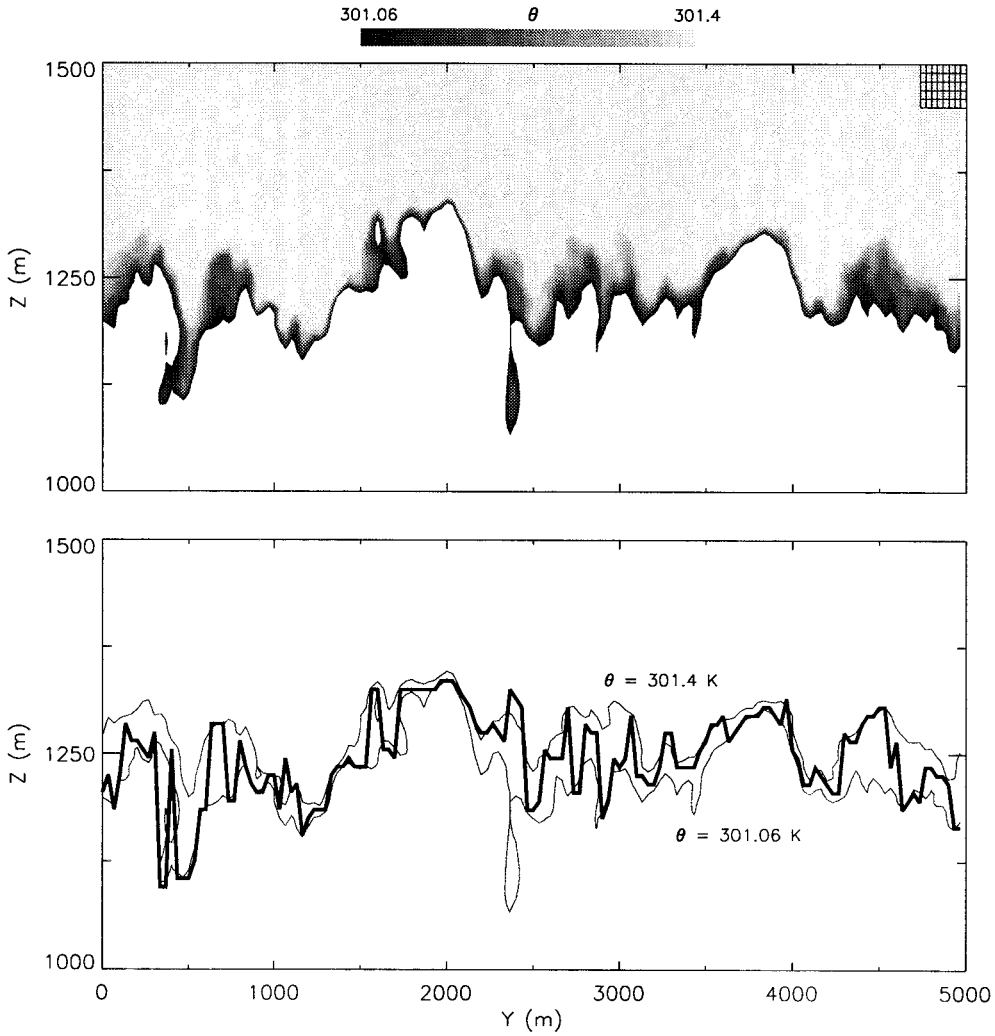

FIG. 7. Upper panel: Visualization of the inversion interface in a y–z plane at $x = 2167$ m using potential temperature contours for case W06. Grayscale color table is shown at top (in K), and mesh spacing is in upper right-hand corner. Note that the grayscale color table picks out only the temperature variations in the inversion region. Potential temperatures lower than 301.06 K in the mixed layer (average $\theta \approx 300.7$ K) appear white. Lower panel: Comparison of local z_i (thick line) from gradient method with maximum and minimum θ contours.

tuating w and θ. Several thermal plume cores can also be clearly identified in the current simulation.

Next, we examine the vertical structure of the inversion layer in the vicinity of an ascending plume. Contours of the instantaneous potential temperature in the range $301.06 \text{ K} < \theta < 301.4$ K in a vertical y–z plane at $x = 2167$ m are shown in the upper panel of Fig. 7. In this figure, the shading is chosen to emphasize the details of the inversion-layer interface. In the lower panel of this figure, the local estimate of $z_i(x, y)$ obtained from the gradient method (see section 4c) is compared with the upper- and lower-temperature contours from the visualization. A strong correlation between the local estimate of z_i and the visualization is observed.

Inspection of the temperature contours shows that the inversion layer has a rich structure. At any particular time (or vertical slice through the domain), domes of fluid from below rise above the nominal inversion height, deep troughs (or pockets) of fluid from above extend down into the PBL, and the thickness of the interface varies over a wide range. From an entrainment perspective, the troughs of fluid that dip down into the PBL are important. These pockets of warm inversion air are possible sites of entrainment in this PBL flow; they are either debris leftover from a previous entrainment event or the site of active entrainment. It should be noted that the horizontal (x–y) and vertical (y–z) views of potential temperature shown in Figs. 6 and 7 are remarkably similar to the flow visualization pictures taken by Deardorff et al. (1980) in a convection tank using a dye tracer.

The inversion layer might be characterized by two

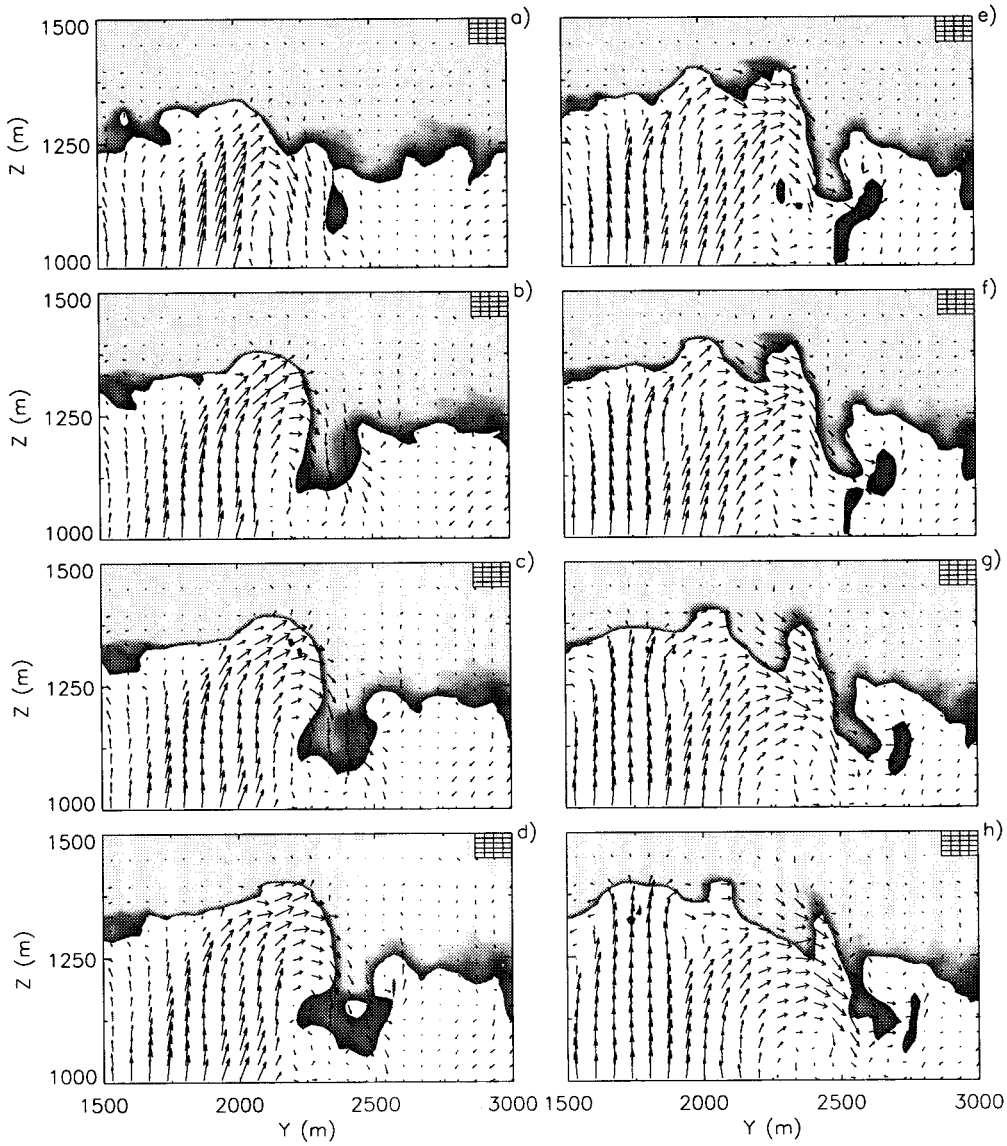

FIG. 8. Temporal and spatial evolution of the inversion interface in a limited domain. Temperature contours as in Fig. 7 along with flow vectors (v, w). Only every third grid point in z and every second grid point in y is shown for clarity. Panels (b)–(h) are 107, 134, 161, 228, 255, 295, and 335 s, respectively, later than (a).

vertical length scales: the local interface thickness Δh and the PBL height z_i. The local interface thickness Δh is defined, somewhat arbitrarily, as the distance between the upper- and lower-temperature contours shown in Fig. 7, that is, the region of dark shading in the upper panel. Figure 7 provides a sense of the typical variability in z_i and Δh at this Ri for example, near $y = 2000$ m $z_i = 1330$ m and $\Delta h < 10$ m, while at $y = 4500$ m, $z_i = 1300$ m and $\Delta h > 100$ m.

In order to study the temporal and spatial evolution of the inversion layer with the goal of identifying entrainment events, we examined in detail various regions of the domain and monitored the flow evolution (3D volumes were sampled frequently enough to make movies). A time sequence is shown in Fig. 8 that starts from the snapshot shown in Fig. 7 and spans about 335 s. Both temperature contours and flow vectors are displayed [here the vector (v, w) is shown at every third grid point]. The spatial and temporal interaction of an active plume with the overlying stable inversion is clearly illustrated.

As the thermal progresses upward the temperature contours at the head of the plume are lifted upward and compressed compared to the average background stratification, that is, $z_i(x, y)$ increases, $\Delta h(x, y)$ decreases, and $\partial\theta(x, y)/\partial z > \partial\langle\theta\rangle/\partial z$. Eventually, the progress of the thermal is stopped by the increasing stratification at the head of the plume and the plume is first deflected

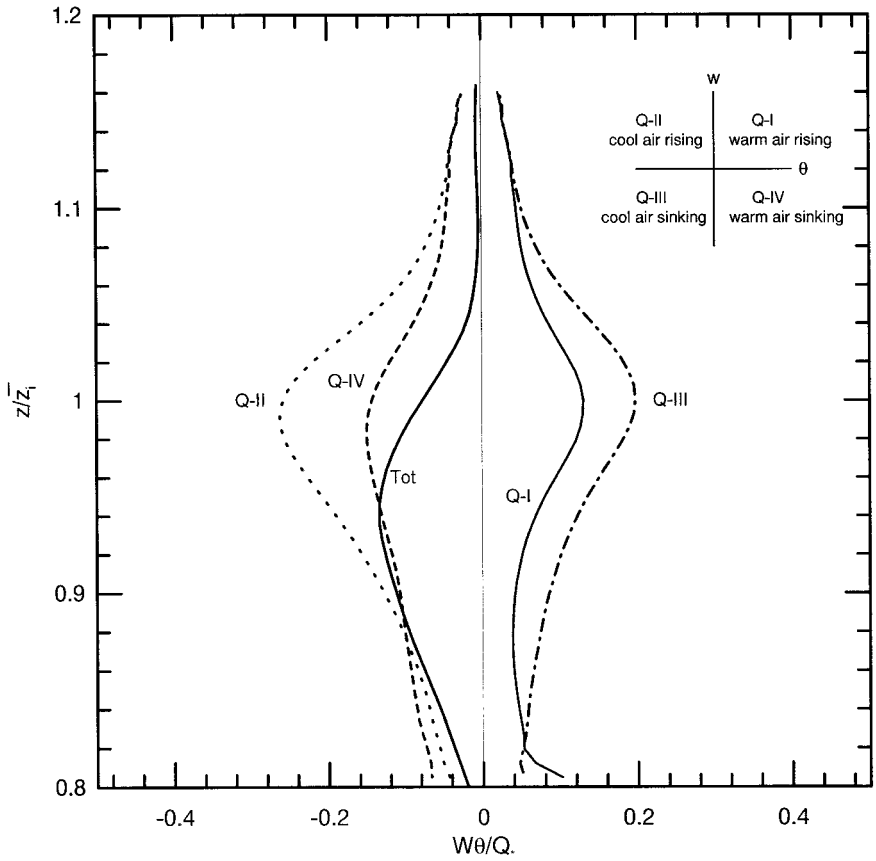

FIG. 9. Profiles of average resolved buoyancy flux partitioned into four quadrants for case W06. Here, QI = $\overline{w^+\theta^+}/Q_o$, QII = $\overline{w^+\theta^-}/Q_o$, QIII = $\overline{w^-\theta^-}/Q_o$, QIV = $\overline{w^-\theta^+}/Q_o$, solid line (Tot) $\overline{w\theta}$.

sideways, in this instance to the right, and eventually downward. The rotational motion that forms inside the plume is sufficiently strong to fold over the interface and draw in warmer fluid from above, resulting in entrainment at the plume's edge, shown clearly in Fig. 8d. Once warm air pockets are drawn down below the nominal inversion height, vigorous turbulent motions can then mix the entrained air throughout the PBL.

The continuing time sequence shown in Figs. 8e–h illustrates another type of entrainment event linked to the interaction of a turbulent thermal and the overlying inversion. Two important consequences of this interaction are the local distortion of the inversion layer; that is, local undulations or pockets are formed in the interface at the edge of the plume, for example, at $y = 2500$ m, and strong horizontal turbulent motions are generated by the deflection of the upward-moving plume. This pocket of warm inversion air that dips below the nominal inversion height is scoured off from the stably stratified air aloft by strong lateral motions as illustrated in Figs. 8e–h. The vigorous horizontal turbulent motions near the edge of the plume pinch off the pocket of warm inversion air located at $y = 2550$ m, thus leading to entrainment.

At this particular Ri, entrainment events like those displayed in Fig. 8 are well resolved with the current mesh (the grid mesh size used in the simulation is indicated in the upper corner of Fig. 8). Although no two events are identical, the scenario displayed in Fig. 8 is typical with entrainment taking place in either a larger-scale engulfment process resulting from a folding of the interface or by a scouring mechanism that pinches off warm air pockets that dip down into the PBL. We also found that the x and y scales of the entrainment events in Fig. 8 are comparable. The entrainment events shown here are remarkably similar to the schematic representation described by Carson and Smith (1974; see their Fig. 1).

b. Quadrant analysis of buoyancy flux, Ri = 13.5

The average minimum heat (or buoyancy) flux $\overline{w\theta}_{\min}$ in the inversion layer is often used as an indicator of net entrainment (see Fig. 3). In order to shed further light on the entrainment process, a quadrant analysis of the heat flux in the inversion layer was performed. Mahrt and Paumier (1984) also used quadrant analysis of the virtual and sensible heat fluxes to examine entrainment. For case W06, we partitioned the resolved LES estimates of the buoyancy flux into the four possible quad-

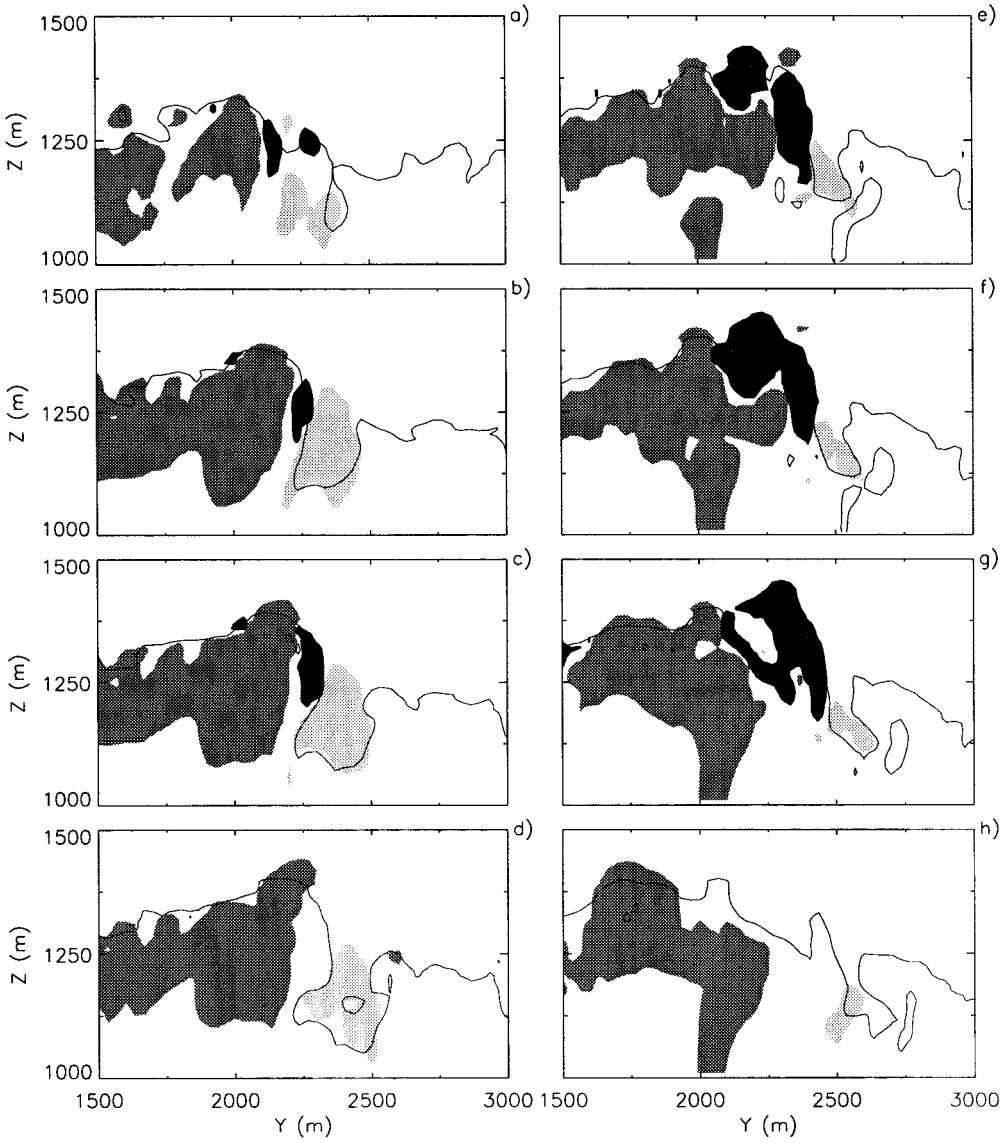

FIG. 10. Temporal and spatial evolution of buoyancy flux for the same flow as in Fig. 8. Light shading quadrant IV flux $w^-\theta^+/Q_o < -0.1$, medium shading quadrant II flux $w^+\theta^-/Q_o < -0.1$, and dark shading quadrant III flux $w^-\theta^-/Q_o > 0.1$. The thin line is the contour $\theta = 301.06$ K, the lowest contour in Fig. 8.

rants, $w^+\theta^+$, $w^+\theta^-$, $w^-\theta^-$, and $w^-\theta^+$, referred to as quadrants I, II, III, and IV, respectively, where $w^+ > 0$, $w^- < 0$, $\theta^+ = [\theta - \langle\theta\rangle] > 0$, and $\theta^- = [\theta - \langle\theta\rangle] < 0$.

Vertical profiles of the average heat flux partitioned according to the four quadrants and the total buoyancy flux are shown in Fig. 9. Note that all fluxes are normalized by the surface heat flux Q_o. There are several features worth mentioning in this figure. First, the absolute peak magnitudes of the individual quadrant fluxes are equal to or greater than the absolute value of the average minimum heat flux; for example, the absolute maximum of the quadrant II flux is more than a factor of 2 bigger than $\overline{w\theta}_{\min}$. Also, notice that the quadrant fluxes reach their absolute maximums at $z = \overline{z_i}$, not at the position of the average minimum buoyancy flux, approximately $z/\overline{z_i} = 0.94$. These observations lead us to conclude that the sum of the larger individual quadrant heat fluxes must be to a large extent self-canceling since $\overline{w\theta} = \overline{w^+\theta^+} + \overline{w^+\theta^-} + \overline{w^-\theta^-} + \overline{w^-\theta^+}$. Furthermore, the boundary between the turbulent layer and the nonturbulent region, that is, $z = z_i(x, y)$ where the temperature gradient is steepest, is a location of vigorous turbulent wave activity in the entrainment zone. From a heat flux perspective $z = z_i$ is a location where quite large opposite signed $w\theta$ fluxes occur. Recall that the most vigorous temperature fluctuations θ' also occur at $z = z_i$, as shown in Fig. 5.

The largest contributors to the average buoyancy flux

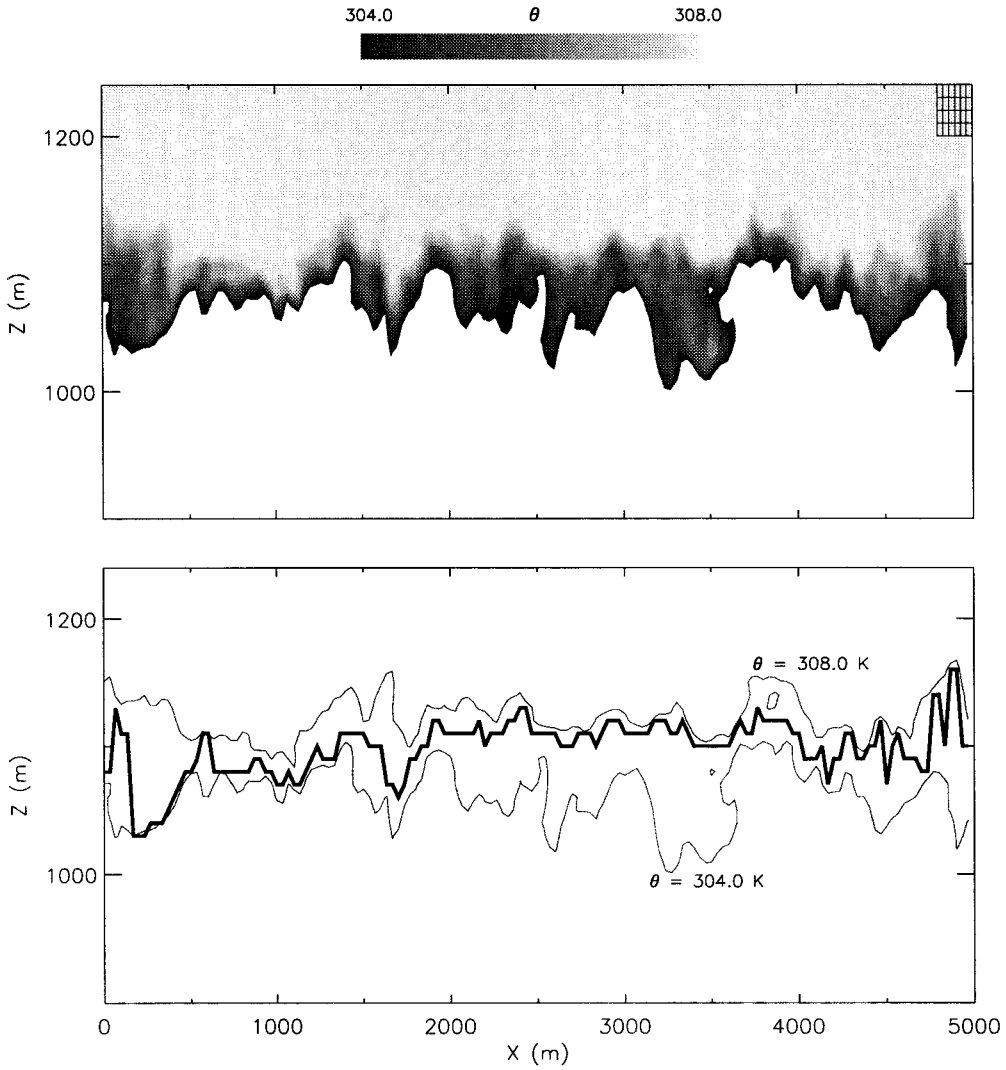

FIG. 11. Upper panel: Visualization of the inversion interface in an x–z plane at $y = 3633$ m using potential temperature contours for case S24. Grayscale color table is shown at top (in K), and mesh spacing is in upper right-hand corner. Lower panel: Comparison of local z_i (thick line) from gradient method with maximum and minimum θ contours.

in the entrainment zone come from quadrants II (upward-moving cooler air) and III (downward-moving cooler air). Our interpretation of this result is that in the entrainment zone upward-moving thermal plumes, which are cool relative to their surroundings, make up a large fraction of the negative heat flux, but because of the stable stratification these same plumes eventually are redirected downward and then become large contributors to positive buoyancy flux. In other words, to a large extent plumes generate a self-canceling buoyancy flux in the entrainment zone. At the position where $\overline{w\theta}$ reaches a minimum value, that is, $z/\overline{z_i} \approx 0.95$, the heat flux from quadrants II, III, and I cancel and $\overline{w\theta}_{\min} \approx \overline{w^- \theta^+}$. Thus, net entrainment is associated mainly with quadrant IV motions, that is, warm air moving downward. For $z/\overline{z_i} > 1$, the buoyancy flux in quadrants IV and I tends to cancel as do quadrants II and III. Wavelike motions above the PBL top where w and θ are $\pi/2$ out of phase would generate this type of cancellation.

Figure 10 shows the temporal and spatial evolution of the heat flux relative to the inversion interface. In this figure, the light, medium, and dark shading corresponds to quadrants IV, II, and III, respectively. The solid line in this figure corresponds to the lowest θ contour in Fig. 8. These results show that the entrainment events identified previously in Fig. 8 do indeed correspond to quadrant IV regions of negative heat flux. Notice that the negative quadrant II heat flux is concentrated in the upward-moving thermal plume and that positive quadrant III results from the plume–interface interaction.

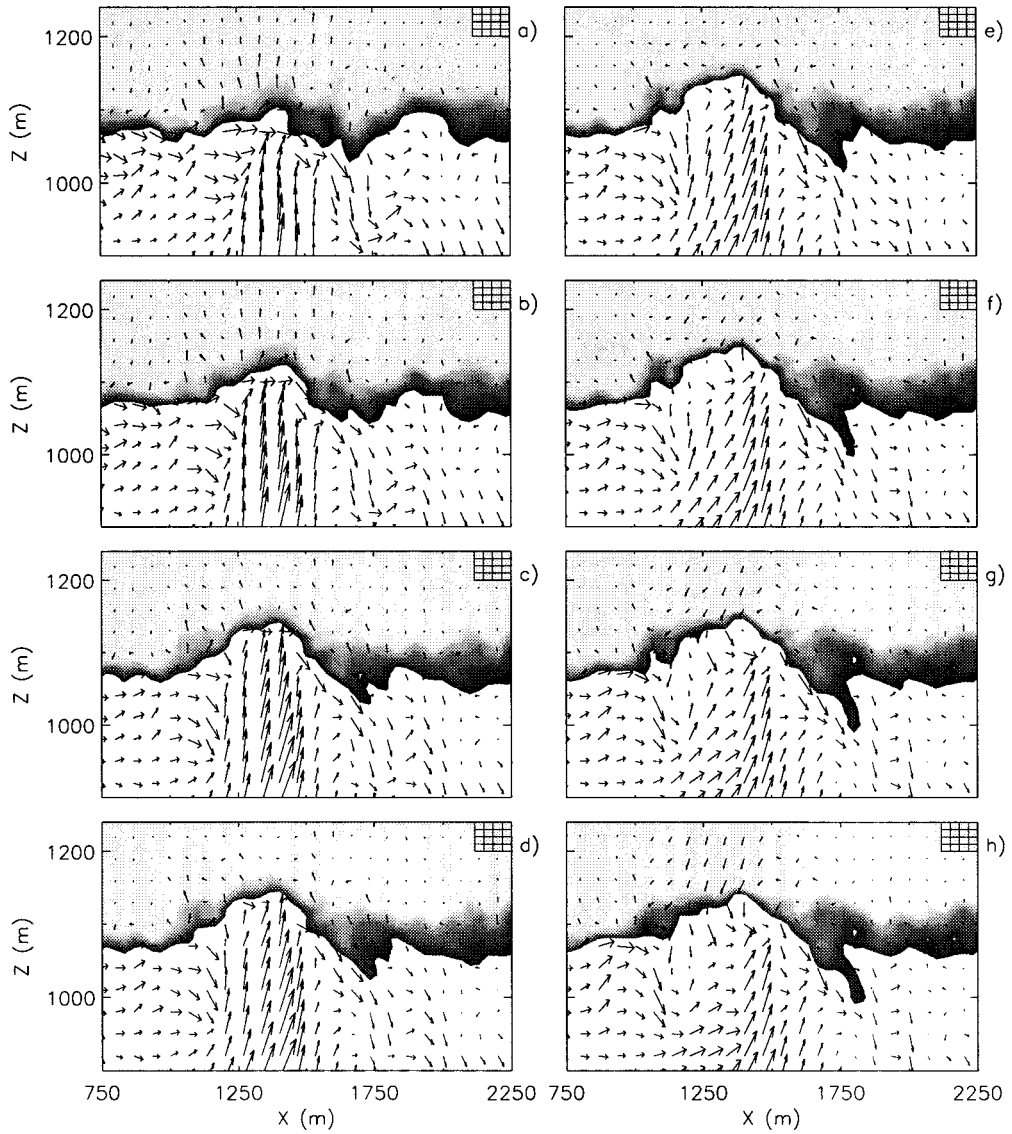

FIG. 12. Temporal and spatial evolution of the inversion interface in a limited domain. Temperature contours as in Fig. 11 along with flow vectors (v, w). Only every third grid point in z and every second grid point in x is shown for clarity. Panels (b)–(h) are 20, 45, 55, 65, 75, 85, and 95 s, respectively, later than (a).

c. Higher Richardson number flow, Ri = 34.5

Laboratory mixing-box experiments (e.g., Perera et al. 1994; Hannoun and List 1988) find that with increasing stratification the entrainment mechanism becomes dominated by what they term intermittent wave breaking. In order to examine whether such events occur in the simulated atmospheric PBL, we conducted a series of LESs at higher values of Richardson number (see Table 2). A typical vertical slice (x–z plane) through the domain showing the structure of the interface at Ri = 34.5 (case *S*24) is given in Fig. 11. Here the potential temperature field is shown using the same technique as in Fig. 7 but over a wider range of temperature contours 304.0 K $< \theta <$ 308.0 K. Qualitatively, the interface at this Ri resembles its counterpart discussed in section 6a but with smaller-amplitude displacements in the interface. The vertical thickness of the interface displays a wide variability and once again pockets of warm inversion air dip down into the PBL, hinting at possible entrainment sites.

In Fig. 12, a sequence of frames depicts the temporal and spatial evolution of the velocity and temperature fields. The interaction of a rising plume and the stable inversion is clearly identified. From these frames the upward motion of the plume simultaneously lifts and thins the inversion similar to what was seen in the low Ri case (e.g., Fig. 8). However, the strong stability of the inversion prevents large-scale folding of the inter-

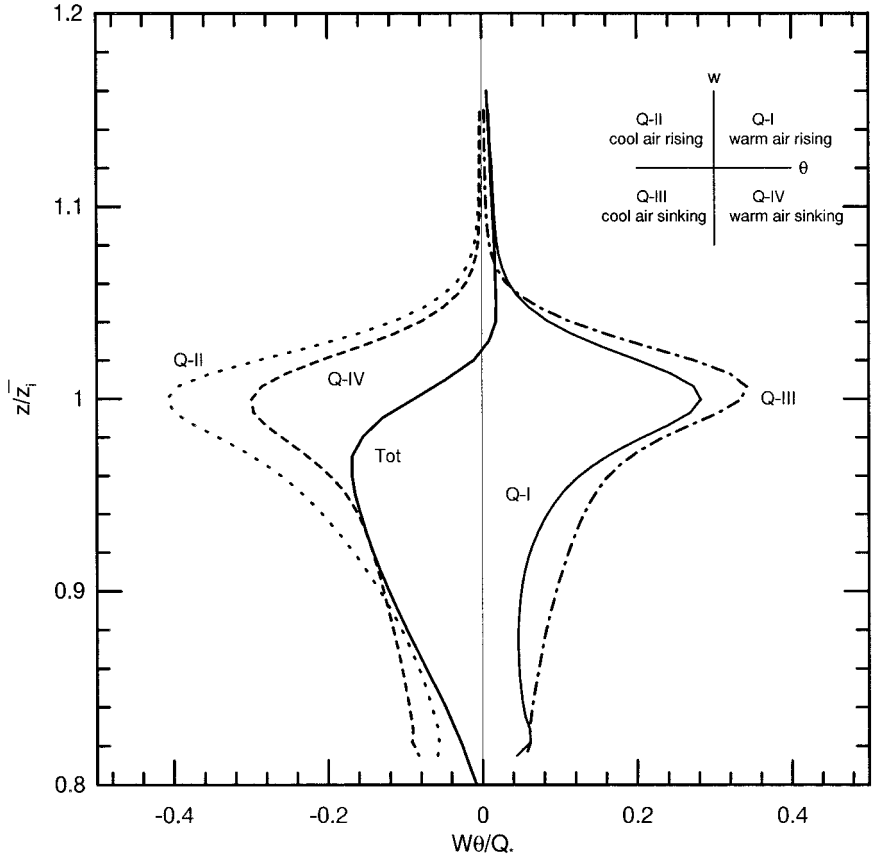

FIG. 13. Profiles of average resolved buoyancy flux partitioned into four quadrants for case S24. Here, QI = $\overline{w^+\theta^+}/Q_o$, QII = $\overline{w^+\theta^-}/Q_o$, QIII = $\overline{w^-\theta^-}/Q_o$, QIV = $\overline{w^-\theta^+}/Q_o$, solid line (Tot) $\overline{w\theta}$.

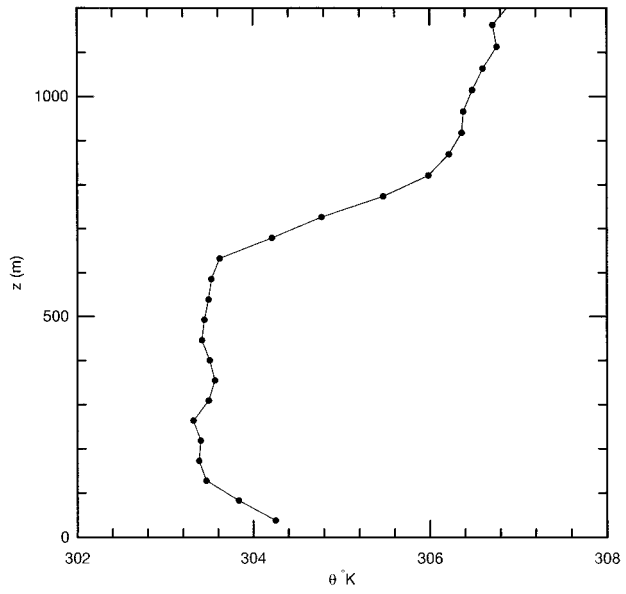

FIG. 14. Profile of virtual potential temperature in the PBL as measured from a radiosonde during the LIFT field experiment on 20 August 1996.

face as shown in Figs. 8a–d. Instead, strong horizontal and downward motions near the plume's edge pull down pockets of warm air similar to the mechanism shown in Figs. 8e–h. These pockets of warm air are stretched out and eventually entrained into the PBL by the same scouring mechanism depicted in Figs. 8e–h. After thorough interrogation of the flow fields at Ri = 34.5 we found numerous entraining events as shown in Fig. 12, but nowhere did the surface exhibit a large-scale overturning as at lower Ri. Also, visualization suggests that intermittent wave breaking is not a primary entrainment mechanism at this Ri.

Results from the quadrant analysis described in section 6b carried out for this case are shown in Fig. 13. In most respects, the quadrant analysis of the buoyancy flux at Ri = 34.5 is quite similar to that at Ri = 13.5. Quadrant II and III buoyancy fluxes predominate but approximately cancel each other. The peak value of each quadrant occurs at $\overline{z_i}$ and clearly above the level of the average minimum heat flux $\overline{w\theta}_{\min}$. At this Ri, the absolute peak value from each of the four quadrants normalized by the surface heat flux is greater than those at Ri = 13.5. The normalized net heat flux, that is, $\overline{w\theta}/Q_o$, at Ri = 34.5 is slightly more negative than at Ri = 13.5 (also see section 7c).

TABLE 3. Properties of LIFT data.

Q_o	0.080 K m s^{-1}
U_{zi}	7.0 m s^{-1}
u_*	0.4 m s^{-1}
$\overline{z_i}$	644 m
w_*	1.19 m s^{-1}
$\overline{z_i}/L$	-10.5
$\Delta\theta$	0.8 K
Ri	≈ 12

d. Comparison with LIFT data

The Lidars in Flat Terrain (LIFT) field experiment provides an opportunity to compare our LES results to atmospheric measurements. LIFT used newly developed lidars with narrow sample volumes and precise pointing capability to gather information about the vertical structure of the PBL. An overview of LIFT is given by Mayor et al. (1997) and Cohn et al. (1998). For our purposes, we have used a small portion of the LIFT dataset that probed the structure of the entrainment zone of a convective PBL using a vertically pointed aerosol backscatter lidar and a nearby radiosonde.

Some of the PBL properties obtained from 1605 to 1625 UTC (midmorning local time) on 20 August 1996 are given in Table 3. The new parameters in Table 3 not previously defined are u_*, the surface friction velocity; U_{zi}, the average wind speed at $\overline{z_i}$; and the ratio of $\overline{z_i}$ to the Monin–Obukhov length L. A vertical profile of potential temperature from the radiosonde is shown in Fig. 14. A well-mixed layer extends up to about 600 m and is limited above by a pronounced stable inversion. Examination of this profile suggests that the maximum $\partial\overline{\theta}/\partial z$ gradient occurs somewhere between 600 and 800 m. Only a rough estimate of the bulk Richardson number can be made since heat flux profiles were not available for accurate computation of the $\Delta\theta$ jump needed in Eq. (1). We estimate that $\Delta\theta \approx 0.8$ K based on the shape of the θ profile in the inversion and assuming a linear profile for $\overline{w\theta}$. Thus, Ri $\approx$ 12. There is a mean wind during this sampling period, but the dominant forcing mechanism is convection since the ratio $\overline{z_i}/L < -10$ (e.g., Moeng and Sullivan 1994). On the basis of the data in Table 3 and the temperature sounding in Fig. 14 we conclude that the PBL at this time of day is similar to the LES experiment W06 at Ri = 13.5 (see Fig. 2).

Measurements from the aerosol backscatter lidar (vertical resolution 3.75 m and temporal resolution 1 s) obtained during the same period as the radiosonde are displayed in Fig. 15. We have displayed the lidar backscatter data in a similar manner as the potential temperature field from LES with the intensity of the gray-scale shading scheme in the upper panel of Fig. 15 chosen to identify the local inversion height. The lidar data is uncalibrated relative backscatter at 1064 nm wavelength. The lidar returns were processed by subtracting the background value and correcting for range dependence. The upper panel of Fig. 15 shows the contrast in scattering at the interface between boundary layer air with high aerosol content and relatively clean air in the overlying inversion. Scattering increases with increasing concentration and size of aerosol particles.

In the lower panel of Fig. 15, estimates of $z_i(t)$ are shown. The lidar backscatter contains many small-scale fluctuations and it was not possible to simply estimate z_i from the maximum gradient as was done for the LES solution. Smooth z_i estimates were obtained by first filtering the lidar signal with a Haar wavelet (e.g., Mahrt 1991) of dilation scale 56 m and then locating the maximum wavelet coefficient, similar to the method described by Mann et al. (1995). The wavelet coefficient is a measure of the gradient in the lidar backscatter signal averaged over the dilation scale.

Overall we are struck by the similarity of the interface structure obtained from the LES and lidar. The lidar measurements show thermal plumes penetrating into the stable inversion layer that tend to sharpen the inversion interface in the region directly above the plumes. Meanwhile, at the edge of the plumes the interface is thicker and pockets of inversion air extend down into the PBL, similar to the LES results. If one compares the inversion height at t = 75 and 300 s the PBL depth varies by as much as 300 m in this time period. The average PBL depth $\overline{z_i}$ = 644 m. In order to estimate the horizontal scale of the inversion interface we invoke Taylor's hypothesis. From Table 3, the winds are about 7 m s^{-1} at the inversion height and hence the 20-min observation period in Fig. 15 corresponds to a horizontal distance of roughly 8400 m. Thus, the horizontal and vertical undulations in the measured PBL interface are of comparable scale to those in the LES experiments. We expect that if the winds aloft were stronger or the surface heat flux smaller, shear effects would dominant and the structure of the inversion layer as well as the entrainment rate would differ from the convectively driven flow investigated here, as suggested by Moeng and Sullivan (1994). In the future we plan to compare LES and lidar measurements for this flow regime as well.

7. Interface statistics and entrainment rate

a. z_i statistics

Averaged statistics of $z_i' = z_i - \langle z_i \rangle$, where z_i is defined using the gradient method, for all the simulations are shown in Figs. 16, 17, and 18. In Fig. 16, the normalized root-mean-square (rms) of z_i, that is, $\sigma_{zi}/\overline{z_i}$, is plotted as a function of the Richardson number Ri. As expected, the fluctuations in z_i are reduced as Ri increases. The data roughly follow a $\sigma_{zi}/\overline{z_i} \sim \mathrm{Ri}^{-1}$ power law. Notice that for nearly the same Ri the use of a monotone differencing scheme produces a larger value of $\sigma_{zi}/\overline{z_i}$ than the second-order centered scheme (compare case S24/m and S24/c). This comes about because the magnitude of the z_i fluctuations are sensitive to the inversion strength. The artificial (numerical) viscosity

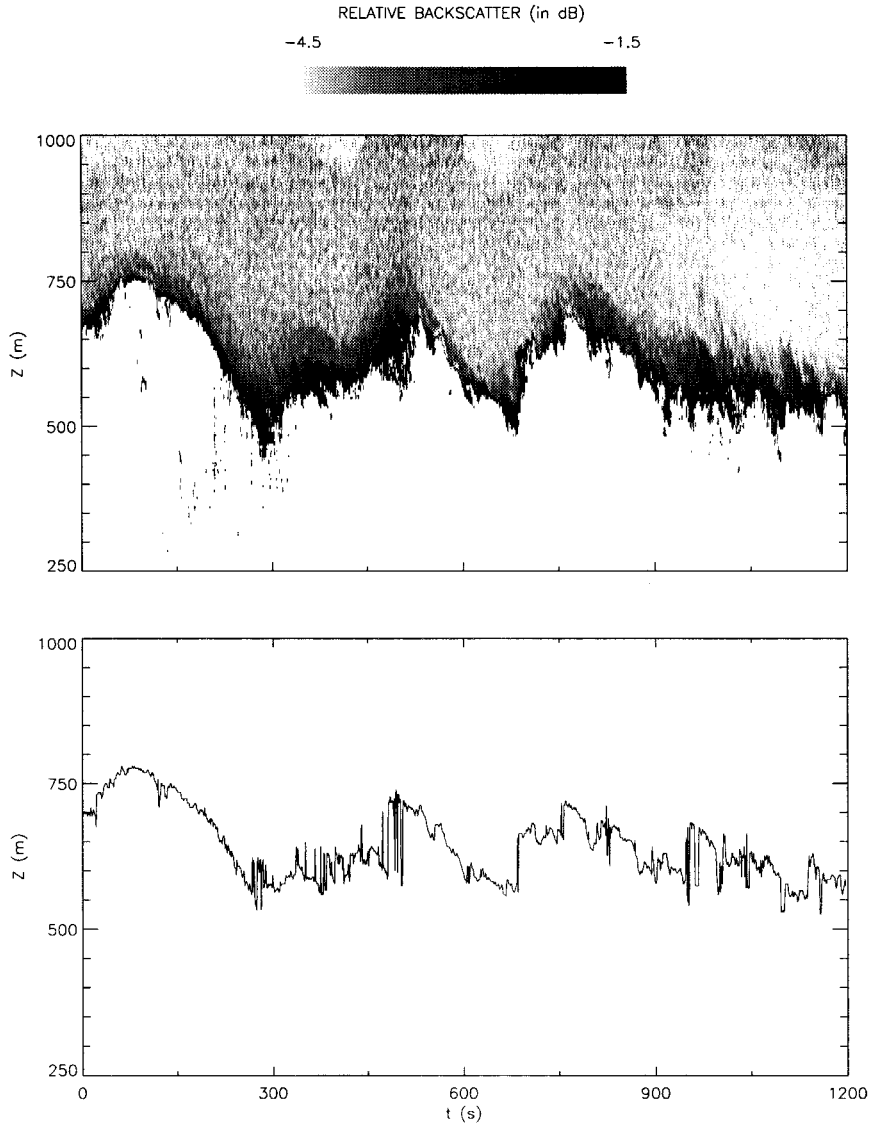

FIG. 15. Upper panel: Vertical profiles of aerosol backscatter in the PBL from a lidar during the LIFT field experiment obtained at the same time as the radiosonde data shown in Fig. 14. Lower panel: Local z_i from wavelet technique.

introduced by the monotone scheme weakens the inversion strength compared to the simulations utilizing the centered finite differencing scheme. For instance, the average maximum gradient in simulation S24/m is about 0.044 K m^{-1} compared to 0.081 K m^{-1} in case *S*24/*c*. At low Ri, the value of $\sigma_{zi}/\overline{z_i}$ is also sensitive to the grid resolution.

In Fig. 17, z_i skewness, $S_{zi} = \overline{z_i'^3}/(\overline{z_i'^2})^{3/2}$, is shown as a function of Ri. Inspection of the figure indicates that the data can be grouped almost bimodally according to the type of inversion, that is, either weak or strong. For Ri < 20, which corresponds to all cases with weak inversions, S_{zi} is positive, whereas those cases with strong inversions (Ri > 20) S_{zi} is small and negative with an approximately linear decrease in skewness with increasing Ri. The large positive skewness for the weak inversion cases is suggestive of intermittency. Our interpretation of these results is that with weak inversions a few vigorous thermals with strong upward motions penetrate well into the overlying capping inversion, thus leading to positive skewness. The flow visualization of the entrainment interface also showed deep penetration of a few thermals into the overlying stratification at low Ri. The strong stratification at high Ri prevents thermals from penetrating very far into the inversion, so that they spread out laterally. At the same time, strong downward motions at the plume edges pull down relatively narrow pockets of warm air well into the mixed layer. The result

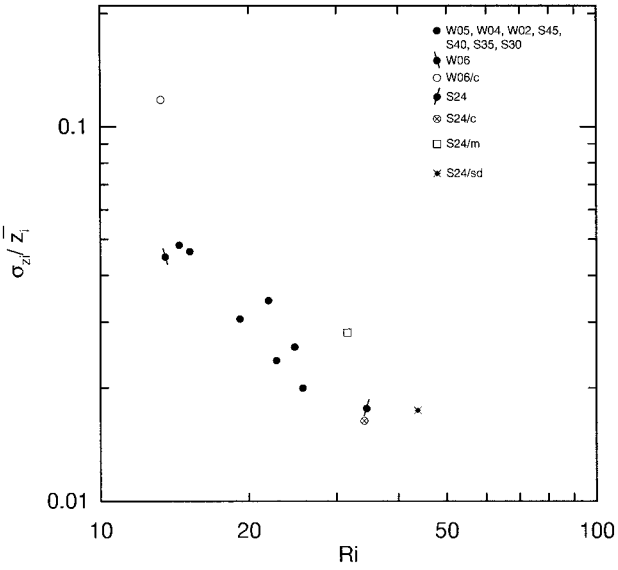

FIG. 16. Normalized rms of z_i fluctuations vs Ri for various LES experiments.

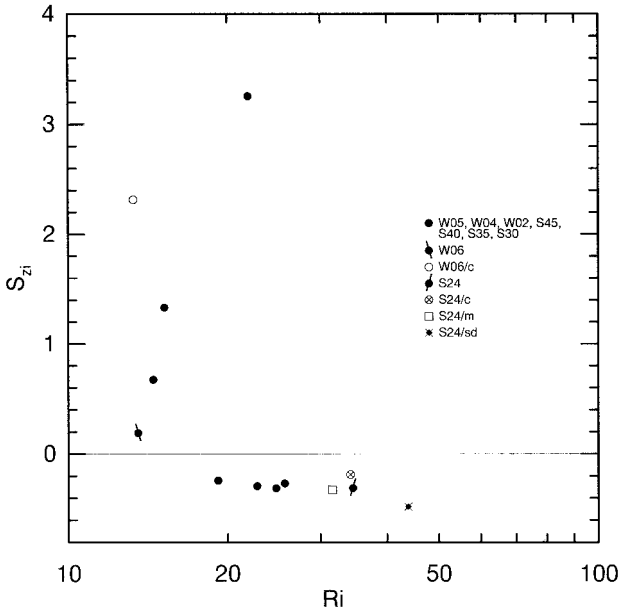

FIG. 17. Skewness of z_i fluctuations vs Ri for various LES experiments.

is a preponderance of wide flat excursions above the mean interface and peaked excursions below the interface, which results in a negative skewness.

One-dimensional longitudinal spectra of the z_i fluctuations, that is, $\psi(\kappa_1)$ where κ_1 is the wavenumber in the x direction, are next shown in Fig. 18. These spectra are obtained by first performing a 2D Fourier transform in a horizontal plane, then summing over all y-component wavenumbers κ_2, and finally averaging over multiple time steps. Examination of the results reveals that for the fine-mesh simulations (W06 and S24) the normalized spectra are qualitatively similar but differ in some quantitative aspects. At the lower Ri (case W06), the spectral slope n in the power law $\psi \sim \kappa_1^{-n}$ gradually varies from about $n = 0.9$ at $\kappa_1 = 0.01$ m^{-1} to $n = 3/4$ at $\kappa_1 = 0.08$ m^{-1}. Compared to the spectrum at lower Ri, $\psi(\kappa_1)$ at Ri $= 34.5$ decays faster and is lower in magnitude beyond $\kappa_1 = 0.007$ m^{-1}. For comparison, Perera et al. (1994) find that the spectra of the interfacial distortions decay like κ_1^{-2} at high wavenumbers in a regime where intermittent wave breaking was observed in their mixing-box experiments. We speculate that our differences in spectral slope are due to different flow conditions; that is, in our LES the PBL turbulence is driven by buoyancy and presumably the effective Reynolds number is larger than that of mixing-box experiments. The z_i spectra from the coarse-mesh simulations are nearly independent of Ri but have noticeably higher fluctuations than the fine-mesh spectra beyond a wavenumber of about $\kappa_1 = 0.01$ m^{-1}. It should be noted, however, that the total z_i variance is greater using the monotone scheme than for the second-order centered method. In general, the spectra of z_i show a dependence on the grid resolution.

b. Entrainment rate

The average entrainment rate (or velocity) $w_e = d\langle z_i\rangle/dt$ was estimated from the $\langle z_i\rangle$ (where z_i is from the gradient method) versus t data using a linear least squares curve fit. Before presenting the entrainment rates, however, it is worthwhile to show the variation of $\langle z_i\rangle$ versus t/τ for different simulations. Typical

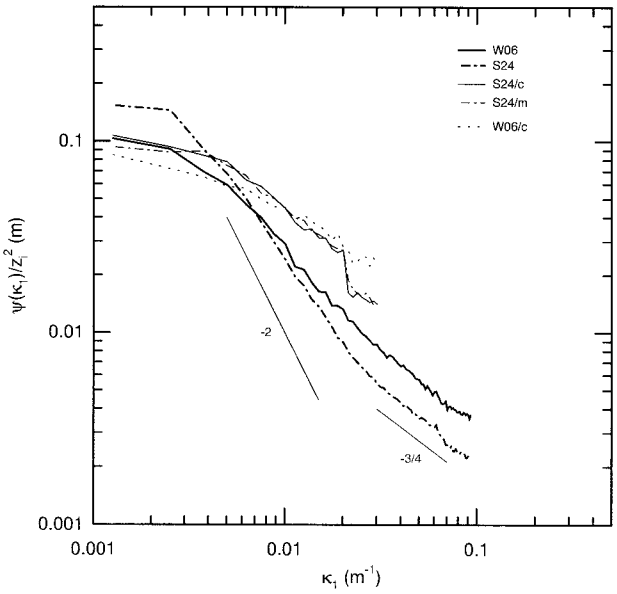

FIG. 18. One-dimensional spectra of z_i fluctuations normalized by $\overline{z_{ig}'^2}$ for different simulations. In mixing-box experiments, Perera et al. (1994) found a κ_1^{-2} spectral slope in the regime where intermittent wave breaking was observed.

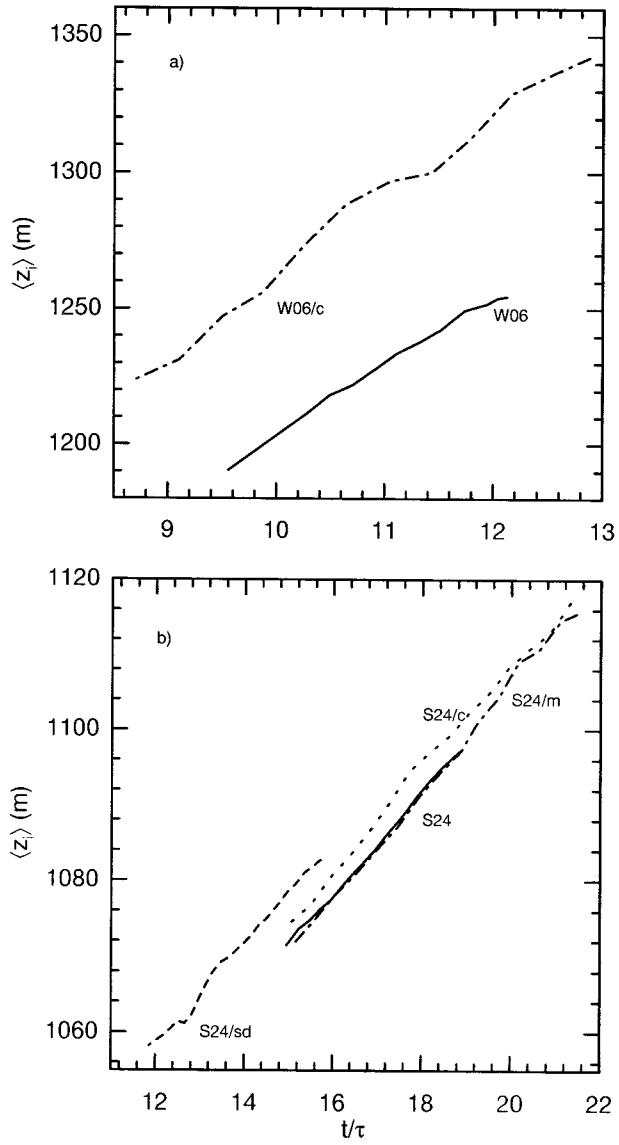

FIG. 19. PBL height as a function of time for simulations with weak and strong stratifications, varying grid resolutions, and different scalar advection schemes: (a) W06 fine mesh and W06/c coarse mesh; (b) S24 fine mesh, S24/c coarse mesh, S24/m coarse mesh and monotone scheme, and S24/sd fine mesh on a smaller domain.

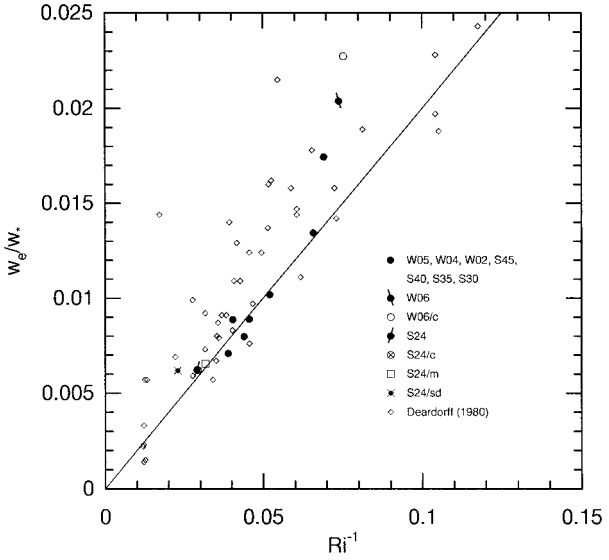

FIG. 20. Comparison of entrainment rate vs Ri^{-1} from current LES calculations and convection tank measurements (Deardorff et al. 1980). The thin line is the curve $w_e/w_* = A\mathrm{Ri}^{-1}$, with $A = 0.2$.

curves are displayed in Fig. 19 for cases at the extremes of our Ri range. In Fig. 19a, results for simulations with weak inversions and different grid resolutions are displayed for cases W06 and W06/c, while Fig. 19b shows results for the strong inversion cases S24, S24/c, S24/m, and S24/sd, which have different grid resolutions and scalar advection schemes.

For the cases with a weak inversion, the results indicate that the coarse-mesh simulation generally predicts a value of $\langle z_i \rangle$ greater than its fine-mesh counterpart at the same dimensionless time. This sensitivity to grid resolution might be expected since the determination of z_i is based on the maximum local gradient $\partial\theta/\partial z$. From our flow visualization, we found that even for weak inversion cases, locally the interface can be quite sharp, which can only be resolved on a fine vertical mesh. Apparently, when coarse meshes are used the average maximum vertical θ gradient is found at a higher z location compared to simulations with a finer mesh. Recall that the spectra of z_i also showed a sensitivity to the grid resolution at small scales. Despite the difference in the absolute value of $\langle z_i \rangle$ on coarse and fine meshes the entrainment rate, that is, the time rate of change of $\langle z_i \rangle$, is about 13% greater for case W06/*c* than for case W06 (see Table 2). Our interpretation of these results is complicated by the fact that Ri also changes slightly with the grid resolution.

The results for the strong inversion cases, displayed in Fig. 19b, are similar to those for weak inversions. Again, coarser meshes tend to have larger $\langle z_i \rangle$; however, the difference between $\langle z_i \rangle$ on coarse and fine meshes is much less because the stratification is stronger. The use of a monotone advection scheme for scalars on a coarse mesh produces results closer to the fine-mesh solution. This is somewhat deceiving since the monotone scheme weakens the maximum vertical θ gradient and this makes the comparison with other S24 cases difficult. Case S24/sd which we could only afford to run for a few turnover times because of the large number of grid points and smaller domain, predicts a slightly higher value for $\langle z_i \rangle$ than the other S24 runs. Case S24/sd uses better resolution than any other case on both its outer and nested grids as well as a smaller computational domain, that is, a domain area that is only 36% as large as case S24 (the horizontal dimensions in S24/sd are 60% of the dimensions in case S24). We speculate that

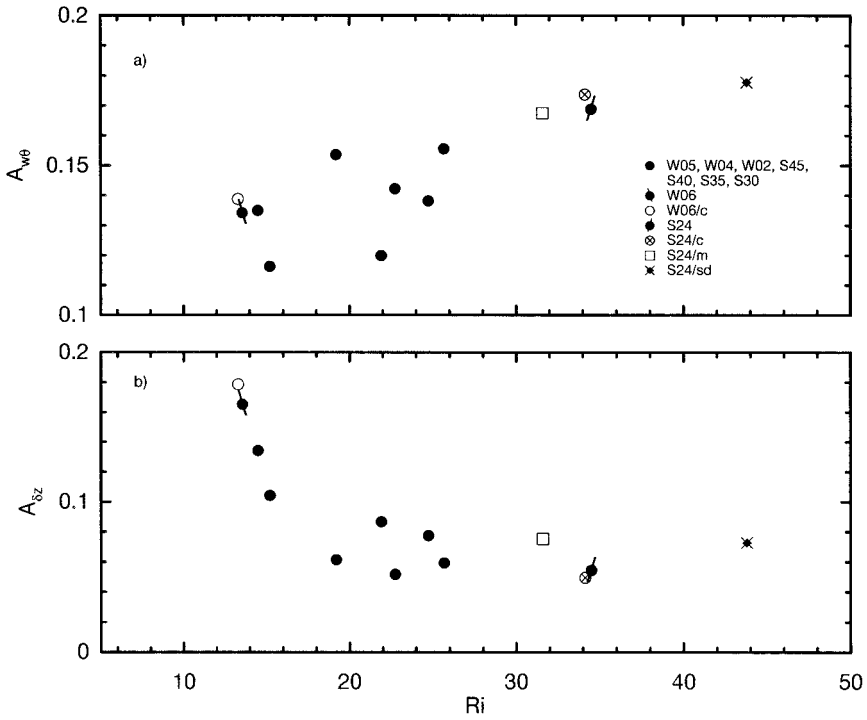

FIG. 21. Terms in first-order jump model for the entrainment rate at the capping inversion of a convective PBL as a function of bulk Richardson number: (a) ratio of minimum buoyancy to the surface heat flux, $A_{w\theta} = -\overline{w\theta}_{\min}/Q_o$, and (b) contribution of finite inversion-layer thickness, $A_{\delta z} = (\delta z/Q_o)\partial\hat{\theta}/\partial t$.

the limited horizontal domain constrains the large-scale plumes to some degree and thereby slightly alters the position of the maximum vertical θ gradient. Overall, the slopes of the curves in Fig. 19b and hence the entrainment rates are quite comparable. The maximum difference for all cases is about 6%.

The dimensionless entrainment rate w_e/w_* variation with Ri^{-1} is next shown in Fig. 20. Also included in this plot are the convection tank measurements of Deardorff et al. (1980). Our computations and the convection tank measurements are plotted in linear coordinates in order to emphasize departures from the entrainment law given by Eq. (3). Several points are worth noting in this figure. First, the entrainment rates estimated from the LESs are in good agreement with the convection tank measurements over the region of common Ri. Close inspection indicates that the convection tank entrainment rates tend to be higher than the LES for the same Ri. The parameter A in Eq. (3) estimated from the LES solution is about 0.2. At $\mathrm{Ri} < 14$, that is, $\mathrm{Ri}^{-1} > 0.07$, the LES results suggest that a different power law might apply to this Ri range. However, the relatively rapid growth of the PBL and the weak inversion in this Ri regime makes it difficult to obtain reliable estimates of the $\Delta\theta$ jump used to compute the Richardson number.

c. *Comparison of LES entrainment rates with a first-order jump condition*

The entrainment rates deduced from our LES are next compared to so-called jump model predictions. Entrainment rate parameterizations are usually developed from the layer-averaged conservation equation for virtual potential temperature by assuming that the potential temperature and the buoyancy flux undergo jumps or discontinuities in the inversion layer. Betts [1974, Eq. (3)] shows that a first-order jump condition for the entrainment rate is

$$w_e\Delta\theta = -\overline{w\theta}_{\min} + \delta z\frac{\partial\hat{\theta}}{\partial t}. \tag{8}$$

In Eq. (8), the inversion layer thickness $\delta z = z_2 - z_1$, where z_1 is the vertical position of the minimum buoyancy flux $\overline{w\theta}_{\min}$, z_2 is the vertical position where the buoyancy flux first goes to zero above z_1, and $\hat{\theta}$ is the average potential temperature between z_1 and z_2, that is, $\hat{\theta} = [\theta(z_1) + \theta(z_2)]/2$. Betts (1974), Deardorff (1979), and recently vanZanten et al. (1998) use Eq. (8) and further assumptions about the inversion layer structure to derive first-order entrainment rate parameterizations that do not involve the time derivative $\partial\hat{\theta}/\partial t$. Note that if the inversion-layer thickness is assumed to be very

thin, that is, $\delta z = 0$ then Eq. (8) reduces to the zero-order jump condition first derived by Lilly (1968). Our intent here is not to develop an entrainment rate parameterization but merely to evaluate the relative contribution of the terms on the right-hand side of (8) to the entrainment rate.

Equation (8) is conveniently written in terms of the bulk Richardson number, defined by Eq. (1) as

$$\frac{w_e}{w_*} = \frac{1}{\mathrm{Ri}}(A_{w\theta} + A_{\delta z}), \tag{9}$$

where the buoyancy flux parameter $A_{w\theta} = -\overline{w\theta}_{\min}/Q_o$ and the inversion-layer thickness parameter $A_{\delta z} = (\delta z/Q_o)\partial\hat{\theta}/\partial t$.

We wish to compare this first-order jump condition with the direct measurements of the entrainment rate shown in section 7b. In order to carry out this comparison, we assume the time rate of change of the average potential temperature $\partial\hat{\theta}/\partial t = \partial\langle\theta_{zi}\rangle/\partial t$, where $\theta_{zi}(x, y)$ is the potential temperature of the inversion-layer height $z_i(x, y)$. This should be a good approximation since we have shown earlier that z_i based on the gradient method is between the position of minimum buoyancy flux z_1 and the height where the flux disappears z_2 (see section 4d). A linear least squares curve fit of the time variation of $\langle\theta_{zi}\rangle$ was used to estimate $\partial\langle\theta_{zi}\rangle/\partial t$.

Figure 21 shows the variation of $A_{w\theta}$ and $A_{\delta z}$ with Ri for all the LES simulations. Clearly, $A_{w\theta} < 0.2$ in the Richardson number range considered, but it has a slightly upward trend with increasing Ri. Meanwhile, the inversion-layer thickness parameter $A_{\delta z}$ displays an opposite trend, decreasing with increasing Ri. Additional LES calculations at higher Ri (not shown) suggest that $A_{w\theta}$ reaches an asymptote near 0.17. However, even higher-resolution LES than used here are needed to study the asymptotic limits of $A_{w\theta}$ and $A_{\delta z}$. One of the noteworthy features shown in Fig. 21 is that the magnitude of $A_{\delta z}$ is not small compared to $A_{w\theta}$ especially at low Ri as is commonly assumed in the zero-order jump model. This is also pointed out by vanZanten et al. (1998).

In Fig. 22, the first-order jump condition given by Eq. (9) is compared with the LES measurements of entrainment rate based on the time variation of z_i. Figure 22c shows that the sum $(A_{w\theta} + A_{\delta z})/\mathrm{Ri}$ is equal to the direct estimates of the entrainment rate. This is a consistency check, since Eq. (9) is a restatement of the conservation equation for virtual potential temperature. Figures 22a and 22b show that for these clear PBLs the direct measurement of w_e/w_* is higher than that predicted by a zero-order jump condition, especially at low Ri. The most important point to draw from these results is that for clear convective PBLs entrainment rate parameterizations derived from a jump condition should account for the finite thickness of the inversion layer.

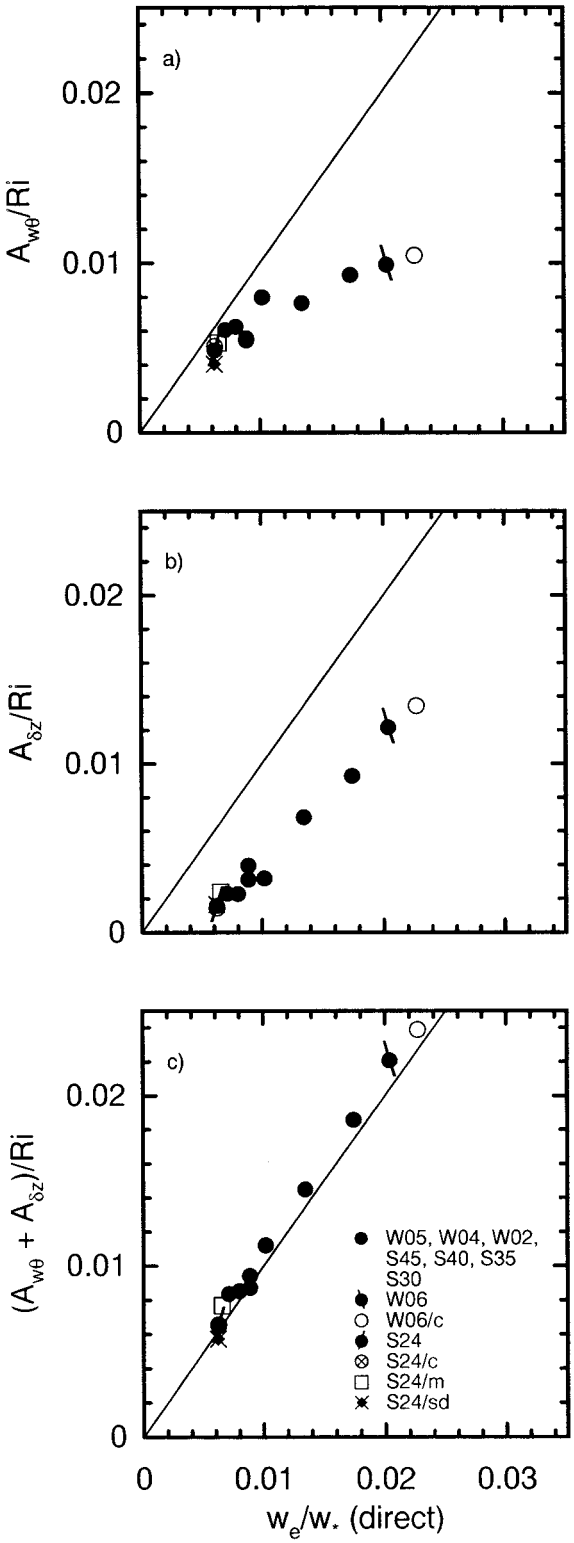

FIG. 22. Comparison of first-order entrainment jump model and direct measurement of entrainment rate for convective PBLs: (a) minimum buoyancy flux contribution $A_{w\theta}$/Ri, (b) finite inversion layer contribution $A_{\delta z}$/Ri, and (c) total contribution $(A_{w\theta} + A_{\delta z})$/Ri. The solid line in each figure represents $w_e/w_*|_{\mathrm{jump}} = w_e/w_*|_{\mathrm{direct}}$.

8. Conclusions

Flow visualization of LES flow fields shows that coherent structures in the convective PBL, that is, thermal plumes, play a crucial role in entrainment mechanics. The interaction of plumes with the stable overlying inversion thins the interface locally and induces strong rotational motions inside the plume. At low Ri, the rotational motions are strong enough to fold the interface and draw in warmer inversion fluid at the plume's edge, thus causing entrainment. At higher Ri, the strong stability of the inversion prevents large-scale folding of the inversion interface, and instead strong horizontal and downward motions near the plume's edge pull down pockets of warm air below the nominal inversion height. These pockets of warm air are then entrained into the PBL by turbulent motions. For the Ri range considered here, intermittent wave breaking found in laboratory experiments is not apparent. The structure of the inversion interface from LES is in good agreement with atmospheric measurements obtained during the Lidars in Flat Terrain field experiment.

A quadrant analysis of the buoyancy flux shows that the interaction of upward-moving thermal plumes with the stable inversion generates both large negative (quadrant II) and positive (quadrant III) buoyancy flux that tend to cancel. The peak value of the quadrant buoyancy flux occurs slightly above the position of the total minimum heat flux. The commonly accepted view of the average minimum buoyancy flux $\overline{w\theta}_{\min}$ as the upper boundary of the PBL underestimates the maximum height of significant turbulent activity in the PBL. Net entrainment is identified with quadrant IV motions $\overline{w^- \theta^+} < 0$, that is, warm air moving downward.

The use of the local maximum gradient in potential temperature to define the PBL height z_i is well correlated with flow visualization of the entrainment interface. Further analysis of z_i indicates that its spatial variance has a power law dependence like Ri^{-1}. The spatial skewness of z_i varies in a bimodal manner depending on the strength of the inversion with weak (strong) inversions having larger positive (smaller negative) z_i skewness. Spectra of z_i show a sensitivity to grid resolution: at high wavenumbers LES with coarse resolutions produce greater z_i fluctuations compared to fine-mesh calculations. The normalized entrainment rate w_e/w_* varies as $A\mathrm{Ri}^{-1}$ with $A \approx 0.2$ and is in good agreement with convection tank measurements. For clear convective PBLs driven by surface heating, the finite thickness of the inversion layer needs to be considered in entrainment rate parameterizations based on jump models.

Acknowledgments. We thank Cees Beets for introducing us to his monotone scheme, Ken Davis for several useful discussions, and Ned Patton, Eileen Saiki, Zbigniew Sorbjan, Jeff Weil, and the anonymous reviewers for their comments on an earlier version of this manuscript. This work was partially supported by the Office of Naval Research and Minerals Management Service through Contract N00014-92-F-0117 and by the National Science Foundation through the National Center for Atmospheric Research.

REFERENCES

Ayotte, K. W., and Coauthors, 1996: An evaluation of neutral and convective planetary boundary layer parameterizations relative to large eddy simulation. *Bound. Layer Meteor.,* **79,** 131–175.

Beets, C., and B. Koren, 1996: Large-eddy simulation with accurate implicit subgrid-scale diffusion. Dept. Numerical Mathematics Report NM-R9601, Utrecht, The Netherlands, 24 pp.

Betts, A. K., 1973: Reply to comment on the paper 'Non-precipitating cumulus convection and its parameterization.' *Quart. J. Roy. Meteor. Soc.,* **100,** 469–471.

Bretherton, C. S., and Coauthors, 1998: An intercomparison of radiatively-driven entrainment and turbulence in a smoke cloud, as simulated by different numerical models. *Quart. J. Roy. Meteor. Soc.,* in press.

Carruthers, D. J., and J. C. R. Hunt, 1986: Velocity fluctuations near an interface between a turbulent region and a stably stratified layer. *J. Fluid Mech.,* **165,** 475–501.

Carson, D. J., and F. B. Smith, 1974: Thermodynamic model for the development of a convectively unstable boundary layer. *Advances in Geophysics,* Vol. 18A, Academic Press, 111–124.

Cohn, S. A., S. D. Mayor, C. J. Grund, T. Weckwerth, and C. Sneff, 1998: The Lidars in Flat Terrain (LIFT) experiment. *Bull. Amer. Meteor. Soc.,* **79,** 1329–1343.

Deardorff, J. W., 1979: Prediction of convective mixed-layer entrainment for realistic capping inversion structure. *J. Atmos. Sci.,* **36,** 424–436.

——, 1980: Stratocumulus-capped mixed layers derived from a three-dimensional model. *Bound.-Layer Meteor.,* **18,** 495–527.

——, and G. E. Willis, 1985: Further results from a laboratory model of the convective planetary boundary layer. *Bound. Layer Meteor.,* **32,** 205–236.

——, ——, and B. H. Stockton, 1980: Laboratory studies of the entrainment zone of a convectively mixed layer. *J. Fluid Mech.,* **100,** 41–64.

Fernando, H. J. S., 1991: Turbulent mixing in stratified fluids. *Annu. Rev. Fluid Mech.,* **23,** 455–493.

Hannoun, I. A., and E. J. List, 1988: Turbulent mixing at a shear-free density interface. *J. Fluid Mech.,* **189,** 211–234.

Hauf, T., and T. L. Clark, 1989: Three-dimensional numerical experiments on convectively forced internal gravity waves. *Quart. J. Roy. Meteor. Soc.,* **115,** 309–333.

Kit, E. L. G., E. J. Strang, and H. J. S. Fernando, 1997: Measurement of turbulence near shear-free density interfaces. *J. Fluid Mech.,* **334,** 293–314.

Klemp, J., and D. Duran, 1983: An upper boundary condition permitting internal gravity wave radiation in numerical mesoscale models. *Mon. Wea. Rev.,* **111,** 430–444.

Koren, B., 1993: A robust upwind discretization method for advection, diffusion and source terms. *Notes on Numerical Fluid Mechanics,* C. B. Vreugdenhil and B. Koren, Eds., Vol. 45, Vieweg-Braunschweig, 117–138.

Lenschow, D. H., 1970: Airplane measurements of planetary boundary layer structure. *J. Appl. Meteor.,* **9,** 874–884.

Lilly, D. K., 1968: Models of cloud-topped mixed layers under a strong inversion. *Quart. J. Roy. Meteor. Soc.,* **94,** 292–309.

Mahrt, L., 1991: Eddy asymmetry in the sheared heated boundary layer. *J. Atmos. Sci.,* **48,** 472–492.

——, and J. Paumier, 1984: Heat transport in the atmospheric boundary layer. *J. Atmos. Sci.,* **41,** 3061–3075.

Mann, J., K. J. Davis, D. H. Lenschow, S. P. Oncley, C. Kiemle, G. Ehret, A. Giez, and H. G. Schreiber, 1995: Airborne observations of the boundary layer top, and associated gravity waves and

boundary layer structure. Preprints, *Ninth Symp. on Meteorological Observations and Instrumentation,* Charlotte, NC, Amer. Meteor. Soc., 113–116.

Mayor, S. D., S. A. Cohn, T. M. Weckwerth, D. H. Lenschow, C. J. Grund, C. J. Senff, R. M. Banta, and R. M. Hardesty, 1997: Lidars in Flat Terrain (LIFT) project overview. Preprints, *12th Symp. Boundary Layers and Turbulence,* Vancouver, BC, Canada, Amer. Meteor. Soc., 5–6.

McWilliams, J. C., P. P. Sullivan, and C.-H. Moeng, 1997: Langmuir turbulence in the ocean. *J. Fluid Mech.,* **334,** 1–30.

Moeng, C.-H., 1984: A large-eddy-simulation model for the study of planetary boundary-layer turbulence. *J. Atmos. Sci.,* **41,** 2052–2062.

——, and J. C. Wyngaard, 1989: Evaluation of turbulent transport and dissipation closures in second-order modeling. *J. Atmos. Sci.,* **46,** 2311–2330.

——, and P. P. Sullivan, 1994: A comparison of shear and buoyancy driven planetary-boundary-layer flows. *J. Atmos. Sci.,* **51,** 999–1022.

Perera, M. J. A. M., H. J. S. Fernando, and D. L. Boyer, 1994: Turbulent mixing at an inversion layer. *J. Fluid Mech.,* **267,** 275–298.

Sayler, B. J., and R. E. Breidenthal, 1998: Laboratory simulations of radiatively induced entrainment in stratiform clouds. *J. Geophys. Res.,* in press.

Schmidt, H., and U. Schumann, 1989: Coherent structure of the convective boundary layer derived from large-eddy simulations. *J. Fluid Mech.,* **200,** 511–562.

Sorbjan, Z., 1996: Effects caused by varying strength of the capping inversion based on a large eddy simulation model of the shear-free convective boundary layer. *J. Atmos. Sci.,* **53,** 2015–2024.

Stevens, D. E., and C. S. Bretherton, 1998: Effects of resolution on the simulation of stratocumulus entrainment. *Quart. J. Roy. Meteor. Soc.,* in press.

Sullivan, P. P., J. C. McWilliams, and C.-H. Moeng, 1994: A subgrid-scale model for large-eddy simulation of planetary boundary-layer flows. *Bound.-Layer Meteor.,* **71,** 247–276.

——, ——, and ——, 1996: A grid nesting method for large-eddy simulation of planetary boundary-layer flows. *Bound.-Layer Meteor.,* **80,** 167–202.

vanZanten, M. C., P. G. Duynkerke, and J. W. M. Cuijpers, 1998: Entrainment parameterization in convective boundary layers derived from large eddy simulations. *J. Atmos. Sci.,* in press.

Wyngaard, J. C., 1984: Large-eddy simulation: Guidelines for its application to planetary-boundary layer research. U.S. Army Research Office Contract 0804, 122 pp.